Gold transport in hydrothermal chloride-bearing fluids: Insights from in situ x-ray absorption spectroscopy and ab initio molecular dynamics

Tagirov, B. R.; Trigub, A. L.; Filimonova, O. N.; Kvashnina, K. O.; Nickolsky, M. S.; Lafuerza, S.; Chareev, D. A.;

Originally published:

December 2018

ACS Earth and Space Chemistry 3(2019)2, 240-261

DOI: https://doi.org/10.1021/acsearthspacechem.8b00103

The chemistry of gold in chloride hydrothermal fluids and melts by X-ray absorption spectroscopy

Boris R. Tagirov[1]*, Alexander L. Trigub[2,5,1], Olga N. Filimonova[1], Kristina O. Kvashnina[3,4], Maximilian S. Nickolsky[1], Sara Lafuerza[3], Dmitriy A. Chareev[6,7,8]

[1] Institute of Geology of Ore Deposits, Petrography, Mineralogy and Geochemistry (IGEM RAS), 35 Staromonetnyi per., 119017 Moscow, Russia

[2] National Research Centre 'Kurchatov Institute', 1 Akademika Kurchatova pl., 123182 Moscow, Russia

[3] ESRF - The European Synchrotron Radiation Facility, CS40220, 38043 Grenoble Cedex 9, France

[4] Helmholtz-Zentrum Dresden-Rossendorf (HZDR), Institute of Resource Ecology, P.O. Box 510119, 01314, Dresden, Germany

[5] Physico-Technical Institute of UB RAS, Kirova st. 132, 426000 Izhevsk, Russia

[6] Institute of Experimental Mineralogy (IEM RAS), 142432 Chernogolovka, Moscow Region, Russia

[7] Ural Federal University, Ekaterinburg 620002, Russia

[8] Kazan Federal University, Kazan 420008, Russia

***Corresponding author:** e-mail tagir@igem.ru, phone +7-499-2308231

Keywords: gold, chloride complexes, hydrothermal fluids, chloride melts, EXAFS, HERFD-XAS

Submitted to Geochimica et Cosmochimica Acta February 2018

ABSTRACT

Chloride-rich fluids are widespread in the Earth's interior from low-temperature subsurface conditions to deep lithosphere. The concentration of chloride salts vary from diluted aqueous solutions peculiar to epithermal deposits to concentrated chloride brines with salinity up to 70 wt% NaCl eq., which coexist with low density vapor during the formation of porphyry systems, and anhydrous (dry) chloride melts at the upper part of degassing magma chamber beneath volcanoes. Here we report an investigation of the speciation of Au in hydrothermal chloride fluids and anhydrous melt by means of X-ray absorption spectroscopy (XAS). The experiments consisted in registration of Au L_3-edge X-ray absorption near edge structure/extended X-ray absorption fine structure (XANES/EXAFS) spectra of Au-bearing fluids in the temperature range from 350 to 575 °C at pressures 0.5-4.5 kbar. The experimental aqueous systems consisted of HCl-, NaCl-, KCl-, or CsCl- dominated fluid (0.02 to 7 mol·(kg H_2O)$^{-1}$) inside a silica glass capillary together with small piece of Au, and SO_2/SO_3 buffer or $K_2S_2O_8$ as a source of oxygen. Spectra of Au dissolved in dry CsCl/NaCl/KCl + $K_2S_2O_8$ melt were recorded at 650 °C. The measured concentrations of Au dissolved in hydrothermal fluids were in close agreement with the values calculated using thermodynamic data available for $AuCl_2^-$. High concentration of Au dissolved in dry chloride melt implies that it can be an effective Au scavenger in natural systems with low H_2O content. It was determined that Au is coordinated by two Cl atoms ($R_{Au\text{-}Cl}$ = 2.25 – 2.28 Å) and 0.2 – 0.6 alkali metal atoms (Me) in the distant coordination sphere of Au at $R_{Au\text{-}Me}$ = 3.3 – 4.1 Å. The presence of the alkali metal cations in the vicinity of Au-Cl complex was confirmed by the XANES spectra registered in High Energy Resolution Fluorescence Detection (HERFD) mode: the white line (WL) intensity decreased substantially in NaCl-dominated fluid and dry melt in comparison with HCl-dominated fluid. The observed decrease of the WL intensity stems from the partial compensation of the positive charge located on Au due to the presence of the distant-coordination-sphere alkali metal cations. The interatomic distances between Au and atoms localized in the first and distant coordination spheres exhibit contrasting behavior with respect to fluid pressure. Increasing pressure

53 results in weak contraction of the first coordination sphere of Au, whereas conjugated increase of
54 the dielectric constant causes expansion of the distant coordination sphere. These results can be
55 explained by the difference in the chemical bond nature. The Cl^- ions in the nearest coordination
56 sphere of Au are bonded to the central atom via the strong (predominantly covalent) chemical
57 bonding, whereas the distant-coordination-sphere cations are weakly bonded to the negatively
58 charged $AuCl_2^-$ complex mostly via the electrostatic interaction. This means that in thermodynamic
59 calculations the dissolution of Au in natural ore-forming fluids, at least of moderate to high
60 densities (> 0.5 $g \cdot cm^{-3}$), can be explicitly described by reactions which involve the formation of
61 $AuCl_2^-$, with mandatory consideration of the effect of weak outer sphere coulomb interactions via
62 the calculation of activity coefficients.

1. INTRODUCTION

Chlorides are the most abundant salt components of hydrothermal fluids in the Earth's crust. The concentration of NaCl, the main electrolyte salt, varies in wide limits, with the average value close to ~ 0.5-1 *m* (see, for example, review of hydrothermal fluid compositions in Seward et al., 2014). In particular, in hydrothermal fluids which formed the volcanogenic massive sulfide (VMS) deposits the chloride concentration ranged from few to 20 wt% NaCl eq. (e.g., Large, 1977; Simonov et al., 2006; Vikent'ev et al., 2009, 2012; Karpukhina et al., 2013). Similar concentrations of chloride salts, with the average value of 4-8 wt% NaCl eq. and maximum concentration up to 26 wt% NaCl eq., were established in hydrothermal vent fluids of black smokers – modern analogues of VMS deposits (Douville et al., 2002; Bortnikov et al., 2004, 2014; Schmidt et al., 2011). Chlorinity of the high-temperature (*t*~600-800 °C) metal-rich fluid rising from a magma chamber in porphyry systems is about 10 wt% NaCl eq. Lowering of the temperature and pressure induces phase separation that results in formation of a low density fluid with salinity of a few wt% NaCl eq. and a brine with salinity of 30-70 wt% NaCl eq. (Heinrich et al., 2004; Sillitoe, 2010; Gregory, 2017). Note that many VMS and porphyry systems belong to the World-class gold deposits with Au resources of more than 100 t. Gold alloys with platinum group elements (PGE: Pt, Pd, Ir, and Rh) are frequent in giant PGE deposits of magmatic origin - deposits of Norilsk, Bushveld, and Stillwater. In all these deposits hydrothermal fluids participated in the formation of PGE-Au mineralization. In the Stillwater Complex the concentration of chloride salts ranged from NaCl-dominated halide melts (>82 wt% NaCl eq., t = 660-800°C) to more complex Na-Ca-K-Fe-Mn-Ba brines of lower salinity (28-79 wt% NaCl eq., t = 480-640 °C, Hanley et al., 2008). Chloride-rich fluids discovered as fluid inclusions in quartz associated with sulfide minerals at Merensky reef (Bushveld complex) were entrapped in the temperature range 750-400 °C. Their salinity varies from high (60-70 wt% NaCl eq.) to moderate-to-low (20 to ~7 wt% NaCl eq.) depending on the entrapment temperature (Ballhaus and Strumpfl, 1986; Zhitova et al., 2016). Abundance of H_2O-, Cl-, and F- bearing minerals crystallized in Norilsk ores in the vicinity of Au chalcogenides,

chlorides, and intermetallic compounds suggested that the Au mineralization was related to the post-magmatic hydrothermal stage which took place at temperature of ~350 °C and below (Sluzhenikin and Distler, 2015).

Native gold crystals and particles are often formed during volcanic eruptions and fumarolic activity. Crystals of native gold were found in products of volcanic eruptions which were formed during 1975-1976 and 2012-2013 eruptions of Tolbachik volcano, Kamchatka (see Chaplygin et al., 2015, and references cited). Micron size native gold particles were discovered on the surface of sulfide minerals (wurtzite-greenockite, (Zn,Cd)S) formed in active fumaroles of Kudriavy volcano, Iturup Island (Chaplygin et al., 2007). High-temperature fumarole gases at these volcanoes, contained both Au (few ppb to few tens ppb) and chloride (as high as 1.2 mol% HCl at Tolbachik volcano, Chaplygin et al., 2015). Association of Au-bearing phases with oxychlorides and chlorides observed in tube precipitates collected at Kudriavy volcano also suggests elevated Au and Cl concentrations in the gas phase (Yudovskaya et al., 2006). Almost dry (anhydrous) chloride salt melt as a reservoir which accumulates metals at the upper part of degassing magma chamber beneath a volcano was suggested by Shmulovich and Churakov (1998) to explain the formation of the metal-rich gas sublimates. High capacity of chloride melts to accumulate Au is demonstrated by their effective usage as a salt flux for the synthesis of crystals (cf. Chareev et al., 2016) and is confirmed in the experiments on the dissolution of Au in (Na,K)Cl melts (Shmulovich et al., 2016). The speciation of Au in melted chloride salts, as well as the dissolution mechanism is, however, unknown.

The chemistry of Au in chloride systems has been experimentally studied via measurements of Au solubility at 300-600 °C and pressure up to 1800 bar (e.g., Zotov and Baranova, 1989; Zotov et al., 1989, 1991, 1995, 2017; Archibald et al., 2001; Stefánsson and Seward, 2003; Guo et al., 2018, and references therein). It was determined that in chloride-bearing acidic fluids Au can be effectively transported in the form of Au-Cl complexes with predominant role of $AuCl_2^-$, even though some inconsistencies still remain regarding the complex stability. The Au speciation model

was confirmed by X-ray absorption spectroscopy (XAS) (Pokrovski et al., 2009). Mei et al. (2014) studied the complexing of Au with chloride in NaCl-rich aqueous fluids by means of *ab initio* molecular dynamics (AIMD) simulations performed at conditions from ambient to 1000 °C, 1500 bar. It was determined that in concentrated NaCl solutions $AuCl_2^-$ is associated with Na^+ ion which is weakly bonded in the outer coordination sphere. The authors proceeded with the calculation of thermodynamic properties of $NaAuCl_2°_{(aq)}$ complex and found that its stability rapidly increases with decrease of the hydrothermal fluid density. These data imply that neutral ionic associates predominate at relatively low densities (d < 0.7 g/cm^3), whereas charged complexes dominate the Au speciation in higher density fluids. At the same time, the dissolved Au concentration measured in the cited above Au solubility studies in the wide range of NaCl/KCl concentrations and fluid densities, including d < 0.7 g/cm^3, can be accurately described without the formation of $Na(K)AuCl_2°_{(aq)}$. In the works of Frank et al. (2002) and Zajacz et al. (2010) the solubility of Au was measured in high-temperature fluids of contrast densities (dense brines with total chloride content of 70 wt% at 800°C, and low density fluids at 1000 °C/1500 bar, respectively). Positive correlations between HCl and NaCl/KCl concentrations with the solubility of Au was observed and interpreted in terms of the formation of $HAuCl_2°$ (Frank et al., 2002) and $NaAuCl_2°$ (Zajacz et al., 2010). However, complex system compositions and the absence of the reliable thermodynamic data on the system's components did not allow the authors to determine the dominant Au complex composition and calculate its stability constant unambiguously.

The aim of this work is to quantify the impact of temperature, pressure, and the system compositions on the chemistry of Au in chloride-rich hydrothermal fluids by means of synchrotron-based XAS. Gold L_3-edge X-ray absorption near edge structure/extended X-ray absorption fine structure (XANES/EXAFS) spectra were recorded in situ for HCl-, NaCl-, KCl-, and CsCl-dominated fluids in the temperature range from 350 to 575 °C at pressures of 0.5-4.5 kbar. The X-ray absorption spectra of dry CsCl/NaCl/KCl melt were acquired at 650 °C. Most of the experiments were performed using the Total Fluorescence Yield (TFY) detection method while the

XANES spectra of two solutions (NaCl- and HCl- dominated), and the dry chloride melt were registered in the High Energy Resolution Fluorescence Detection (HERFD) mode (Glatzel and Bergman, 2005). The presence of cation was detected in the second coordination sphere of Au for alkali metal – dominated fluids and melts. Despite the fact that geometry of the distant coordination sphere is highly disordered, we found that the outer-sphere cation affects the charge state of Au. The contrast effect of pressure was determined on interatomic distances between Au and atoms localized in its nearest and distant coordination spheres.

2. METHODS

2.1. X-ray absorption spectroscopy

X-ray absorption experiments were performed at the European Synchrotron Radiation Facility (ESRF) in Grenoble, France. The Au L_3-edge TFY XAS (XANES/EXAFS) spectra were recorded at the Rossendorf Beamline BM20 (ROBL). The storage-ring operating conditions were 6.0 GeV and 80-100 mA. The photon energy was scanned from 11620 to 12670 eV using the Si(111) monochromator coupled to Rh-coated mirrors for the collimation and reduction of higher harmonics. Energy calibration was performed using the L_3-edge excitation energy of Au metal foil (11919 eV). The TFY XAS spectra were collected using 13-element high-throughput Ge-detector. The total energy resolution (incident energy and core − hole lifetime broadening) has been evaluated as 8.8 eV. The detected intensity was normalized to the incident photon flux.

The Au L_3-edge HERFD-XANES spectra were collected at the high-brilliance X-ray absorption/X-ray emission spectroscopy undulator beamline ID26 (Gauthier et al. 1998). The ring current was varied between 150 and 200 mA. The incident energy was selected using the <111> reflection from a double Si crystal monochromator. Rejection of higher harmonics was achieved by three Pd mirrors positioned at an angle of 2.5 mrad relative to the incident beam. The incident X-ray beam had a flux of approximately $2 \cdot 10^{13}$ photons s^{-1} on the sample position. The spectra were measured in the HERFD mode using an X-ray emission spectrometer (Glatzel and Bergman 2005;

Kvashnina and Scheinost 2016). The sample, analyzer crystal and photon detector (silicon drift diode) were arranged in a vertical Rowland geometry. The Au L_3-edge HERFD-XAS spectra were obtained by recording the intensity of the Au $L_{\alpha 1}$ emission line (9713 eV) as a function of the incident energy. The emission energy was selected using the <555> reflection of four spherically bent Ge crystal analyzers (1 m curvature radius) aligned at 78° Bragg angle. A combined (incident convoluted with emitted) energy resolution of 1.5 eV was determined as the full width at half maximum of the elastic peak. The intensity was normalized to the incident flux.

The experimental set-up used for the high-temperature in situ XAS experiments is described in detail in Trigub et al. (2017a,b) and will be only briefly outlined here. The heating experiments were performed using a capillary technique initially developed for Raman spectroscopic studies (Chou et al., 2008, 2012; Ding, 2010). A small piece of Au wire (1.2-1.5 mm long) was loaded into a Polymicro Technologies™ silica glass capillary: 600 μm OD, 250 μm ID, 12 mm length (BM20 beamline), or 600 μm OD, 400 μm ID, 15 mm length (ID26 beamline). The capillaries were filled with experimental solutions and hermetically sealed (the capillaries were water-cooled during the sealing). The redox state of the system was controlled either by sulfite/sulfate equilibrium (a solution with known concentration of SO_2/H_2SO_4 or Na_2SO_3/H_2SO_4 was loaded into the capillary), or by oxygen produced due to the thermal decomposition of $K_2S_2O_8$ ($K_2S_2O_8 \rightarrow K_2SO_4+SO_2+O_2$). In the latter case a weighted amount (~0.02-0.2 g) of KCl + $K_2S_2O_8$ mixture was loaded into the capillary prior to an experimental solution. The HCl concentration was determined by volumetric titration against Trizma® base using methyl red as indicator, the concentration of SO_2 - by iodometric titration, and the concentration of H_2SO_4 by densimetry. In case of dry chloride melt the capillaries were loaded with the eutectic mixture of CsCl/NaCl/KCl (30 at% NaCl/24.5 at% KCl with melting temperature of 478°C (Fullam, 1971) together with $K_2S_2O_8$. The volumetric ratio of the chloride mixture to $K_2S_2O_8$ was ~ 10/1. The capillaries with eutectic chloride mixture were evacuated down to a 10^{-4} bar pressure, sealed, and preconditioned at the experimental temperature during 24 hours. At the beamline a capillary was placed into the microtomography furnace (Bellet

et al., 2003) between two plates of silver (BM20 beamline) or stainless steel (ID26 beamline) which eliminated temperature gradient. Temperature readings were calibrated before the experiments at an accuracy of ±5 °C with a *K*-type thermocouple inserted directly in the place of the capillary. Pressure inside the capillary was estimated from the degree of filling of the capillary using *PVT* properties of H_2O-NaCl system (Driesner, 2007; Driesner and Heinrich, 2007) or, in case of HCl-dominated fluids, H_2O-HCl (Bach et al., 1977). We estimate the uncertainty of the calculated pressures as ±10% for HCl- and NaCl-dominated fluids, and ±25% for KCl- and CsCl- dominated ones. The spectra were recorded after thermal equilibration of the experimental system and the signal stabilization. Usually ca. 30-45 min at the experimental temperature was necessary to attain the stationary state. The parameters of XAS experiments and the experimental system compositions are listed in Table 1.

2.2. EXAFS spectra fitting and wavelet transforms

The EXAFS ($\chi_{exp}(k)$) data were analyzed using ARTEMIS program (a part of IFEFFIT software package, Ravel and Newville, 2005). Following standard procedures for pre-edge subtraction and spline background removal, the structural parameters - interatomic distances (R_i), coordination numbers (N_i), and Debye–Waller factors (σ^2_i) - were determined via the non-linear fit of the theoretical spectra to the experimental ones with the equation

$$\chi(k) = S_0^2 \sum_{i=1}^{n} \frac{N_i F_i(k)}{R_i^2 k} e^{\frac{-2R_i}{\lambda(k)}} e^{-2\sigma_i^2 k^2} \sin\left(2kR_i + \varphi_i(k)\right) \quad . \qquad (1)$$

The theoretical spectra were simulated using photoelectron mean free path length $\lambda(k)$, amplitude $F_i(k)$, and phase shift $\varphi_i(k)$ parameters calculated *ab initio* using the program FEFF6 (Zabinsky et al., 1995).

Wavelet transform (WT) analysis of the EXAFS spectra was performed as described in Penfold et al. (2013), Timoshenko and Kuzmin (2009), Funke et al. (2007). The WT consists in replacement of the infinitely expanded periodic function in Fourier transform by a local function -

the wavelet. The WT allows analyzing the experimental EXAFS spectra in two-dimensional k/R space and enables separation of the contributions from atoms with different Z. The WT of a given signal $\chi(k)$ is defined as

$$W_f^{\psi}(a,k') = \frac{1}{\sqrt{a}} \int_{-\infty}^{+\infty} \chi(k) \psi^* \left(\frac{k-k'}{a} \right) dk \quad , \quad (2)$$

where the scalar product of the EXAFS signal and the complex conjugate of the wavelet (ψ^*) is calculated as a function of a and k'. The a parameter is related with R as $a = \frac{\eta}{2R}$, and k' conforms to localization of the wavelet function in k-space. In this work we used the WT based on the Morlet wavelet functions

$$\psi(k) = \frac{1}{\sqrt{2\pi}\sigma} e^{i\eta\eta} e^{-k^2/2\sigma^2} \quad , \quad (3)$$

where parameters σ and η are width and frequency of the wavelet function, respectively. These parameters should be adjusted to get appropriate resolution in k- and R-space. For providing better quality of WT images we used modified WT functions (Timoshenko and Kuzmin, 2009).

2.3. *Ab initio* molecular dynamics (AIMD) simulations

The AIMD simulations are aimed to facilitate the interpretation and modeling of XAS results. Details of the AIMD simulations are described in Trigub et al. (2017b). Born–Oppenheimer AIMD simulations were performed with the aid of CP2K program package (VandeVondele et al., 2005). A hybrid Gaussian plane-wave method (GPW) (Lippert et al., 1997) was used. The Goedecker–Teter–Hutter (GTH) norm-conserving pseudo-potentials (Goedecker et al., 1996; Hartwigsen et al., 1998; Krack, 2005) were applied to replace core electrons. The electronic density cut off was set at 500 Ry. For all the atoms the Double-zeta valence plus polarization (DZVP) basis set optimized for molecular geometries was used. The spin polarized general gradient approximation by Perdew−Burke−Enzerhof (PBE) (Perdew et al., 1996) augmented with a correction of the van der Waals (vdW) interactions was applied as exchange correlation functional,

the nonlocal rVV10 vdW functional was used (Vydrov et al., 2009; Sabatini et al., 2013). The *b* parameter which determines the nonlocal behavior of the functional was set to 9.3 according to Miceli et al. (2015). The simulations were conducted in the canonical *NVT* ensemble, with the simulation time step of 0.5 fs and periodic boundary conditions. The AIMD trajectory was accumulated for 20 ps and 10 ps for solution and melt, respectively. Each AIMD calculation was preceded by equilibration phase of 5 ps. The temperature was controlled via a Nosé–Hoover chain thermostat (Nosé, 1984a, 1984b). Starting configurations for AIMD calculations were generated by classical MD method with the aid of GROMACS software (Berendsen et al., 1995). The system contained $AuCl_2^-$ or *Cat*[$AuCl_2$] complex (*Cat* = H, Na, K, Cs) which geometry was optimized with Gaussian 09 suite of programs (Frisch et al., 2016) (the Møller-Plesset Perturbation Theory (MP2) was applied; solvation effects were accounted for by means of the Conductor-like Polarized Continuum Model (CPCM), see Pokrovski et al. (2009) for calculation details). Details of the chemical system compositions, box sizes, and temperatures used in the simulations are given in Table 2.

An additional calculation was performed to check the effect of basis set size on results of the AIMD calculation. Calculation H (Table 2) was identical to calculation E in terms of the atomic system parameters (system composition, box size), but was performed with triple-zeta valence basis set (TZV2P) applied for all atoms. This calculation was performed only for one system because the calculation time increased substantially (from 25 s to 40 s for one time step).

Results of AIMD calculations are presented in the form of plots of atomic densities and coordination numbers. The radial density $\rho(R)$ of surrounding atoms is related to coordination numbers via expression:

$$N(R) = \int 4\pi r^2 \rho(R) dr \ . \qquad (4)$$

2.4. EXAFS and XANES spectra simulations using AIMD data

Every 50 fs of AIMD simulation snapshots of atomic configurations were extracted and used to calculate Au L_3-edge EXAFS/XANES spectra (hereafter the AIMD-EXAFS/AIMD-XANES notation will be used for the calculated spectra). The configuration-averaged Au L_3-edge EXAFS spectra were calculated using FEFF8.5L program (Ankudinov et al., 1998). The Au-Cl distances were corrected by a factor of 0.97 to account for differences between experimental (EXAFS) and theoretical (AIMD) radii of the first coordination sphere. The multiple scattering (MS) contributions to EXAFS were accounted up to the fifth order within a cluster of 6 Å radius around the absorbing atom. The calculation of the cluster potential was performed for every geometry configuration. The self-consistent complex exchange-correlation Hedin–Lundqvist potential and default values of muffin-tin radii as provided within the FEFF8.5L code were applied. The amplitude of the theoretical EXAFS spectrum was multiplied by the $S_0^2 = 0.84$ factor as determined from the Au_2S EXAFS spectra fitting.

Theoretical calculations of the Au L_3-edge HERFD-XANES spectra were performed using the finite difference method (FDM) by means of FDMNES program (Joly, 2001; Guda et al., 2015). Relativistic self-consistent field (SCF) FDMNES calculations were carried out with the exchange-correlation part of potential in a local density approximation (Hedin and Lundqvist, 1971). The final electronic states were calculated in a full core hole screening. Atomic clusters inside the spheres with radii of 6 Å were chosen for both SCF and FDM XANES calculations. Many-body effects and core-hole lifetime broadening were accounted for by means of arctangent convolution (Bunău and Joly, 2009).

2.5. Bader charges calculation

The atomic clusters obtained by means of AIMD simulations were used to study the charge state of Au. First, the electron density of each cluster was calculated by means of Quantum Espresso software package (Giannozzi et al., 2009). At this stage we applied a projector-augmented wave (PAW) method with norm-conserving pseudopotentials and the Perdew-Burke-Ernzerhof (PBE)

exchange-correlation functional. The SCF method was applied with a 100 Ry kinetic energy cutoff for the plane waves and an SCF tolerance better than 10^{-9} for the electronic structure calculations.

Atomic charges were determined according to quantum theory of atoms in molecules (QTAIM, Bader, 1990, 1991). The local atomic charges of Au were calculated by integrating the charge density within a Bader volume around the atom using Critic2 software (Otero-de-la-Roza et al., 2009, 2014).

3. RESULTS AND DISCUSSION

3.1. Quantitative analysis of XANES spectra and dissolved Au concentrations

Gold L_3-edge HERFD-XANES spectra are shown in Fig. 1, and the TFY-XANES spectra are presented in Fig. 2a,b. Positions of the main spectral features are given in Table 3. In all considered systems the oxidation state of Au is +1 despite high oxygen fugacity, especially in the experiment with chloride melt. The HERFD-XANES spectra of chloride melt, NaCl- and HCl-rich solutions differ in the height of the white line (WL, the first, most intense feature). The most intense WL was observed in experiment cap28 with HCl-dominated fluid (3*m* HCl/0.02*m* NaCl, Fig. 1). The WL's intensity of NaCl-rich fluid in cap30 experiment (3*m* NaCl) and dry chloride melt (cap5407) are considerably lower. The Au L_3-edge absorption is related to the 2*p*-5*d* dipole-allowed transitions: $2p_{3/2} \rightarrow 5d_{5/2}/5d_{3/2}$. Therefore, the WL intensity reflects the number of empty states (holes) in $5d_{5/2}$ and $5d_{3/2}$ orbitals above the Fermi level. Low WL intensity of NaCl-rich fluid and chloride melt indicates the reduced unoccupied density of states (DOS) of Au 5*d* orbitals, or, in other words, larger number of electrons localized at Au 5*d* orbitals for salt-rich systems (cap30 and cap5407) than in the HCl-dominated system (cap28). This fact can be quantitatively explained by interaction of positively charged ions with $AuCl_2^-$ complex in concentrated salt fluid and melt. The presence of positively charged ions in the vicinity of $AuCl_2^-$ complex results in electron transfer from ligands to metal, which gives rise to decrease of the number of holes in Au 5*d* orbitals (or decrease of the positive charge localized on Au) and, therefore, decrease of the WL intensity. The

319 decrease of the positive charge is confirmed by the Bader partial atomic charges calculation which
320 is discussed below (section 3.5).

321 The WL intensities of the TFY XANES spectra of hydrothermal fluids (cap122, cap118,
322 cap117, cap110), all of which were recorded for salt-rich systems, are identical (Fig. 2a). At the
323 same time, the WL of the TFY XANES spectrum of salt melt (cap2156) is more intense than WL of
324 K- and Cs-bearing aqueous fluids. This fact can be explained by more effective compensation of Au
325 positive charge in aqueous fluids which contain high concentrations of heavy alkaline metal cations
326 in comparison with chloride salt melt. Besides, according to the AIMD calculations, the positive
327 charge on Au in chloride melt increases due to the presence of Cl^- ions in the distant coordination
328 sphere at 2.6 – 3 Å, whereas no Cl^- ions were detected in the second coordination sphere of Au in
329 aqueous fluids (see section 3.3). We note, however, that the effect of fluid composition on the
330 electronic density distribution within the Au complex and on the Au valence state remains open.

331 Figure 2b compares XANES spectra of chloride melt (cap2156) recorded at high and
332 ambient temperature. The spectra are different: the crystallized melt spectrum exhibits several
333 additional features which are absent in the high-temperature spectra. This difference is connected
334 with appearance of long-range atomic order in crystallized melt. The edge jump (e.j.) and WL
335 positions of these spectra are also shifted relative to each other (Table 3).

336 The concentrations of dissolved Au calculated from the amplitude of the absorption edge
337 height of the transmission spectra are listed at the bottom of Table 1. They are in close agreement
338 with Au solubilities calculated using thermodynamic properties of $AuCl_2^-$ reported in Akinfiev and
339 Zotov (2010). Good agreement between results of our experiments and calculated solubilities
340 argues for high quality of the thermodynamic model of Akinfiev and Zotov (2010), as well as the
341 experimental data which were used by the authors to calculate thermodynamic properties of $AuCl_2^-$.
342 Note that relatively high uncertainty of Au concentrations determined in the present study, which
343 we estimate as ± 0.3 log units, stem from the spherical shape of the capillary, possible shift of the
344 beam from the center of the capillary, uncertainty in the solute concentrations due to weighting of

small masses of solid reagents added directly to the capillaries, and due to possible loss of volatile components during the sealing of the capillary. These uncertainties can account for the underestimated experimental Au solubilities compared to those calculated using database of Akinfiev and Zotov (2010).

We estimate the concentration of Au dissolved in chloride melt as ~ 1 wt%. This concentration (in mol fraction scale) is ca. 10 times lower than the concentration of oxygen produced by decomposition of potassium persulfate. However, it is more than likely that the equilibrium Au concentration has not been attained due to slow kinetics of Au dissolution in chloride melt: we were not able to detect dissolved Au during one hour XAS experiment preformed at 650 °C with capillaries which were not subjected to preconditioning. Therefore, we can conclude that the solubility of Au in chloride melts can be very high, but the quantitative thermodynamic description of the Au solubility needs further experimental examination.

3.2. EXAFS spectra fitting

Roughly speaking, temperature, pressure, and the experimental system composition have little effect on the shape of Au L_3-edge EXAFS spectra and their Fourier transforms (at least at k < 10 Å^{-1} and R < 3 Å, Fig. 3a and b, respectively). Results of EXAFS spectra fitting preformed by means of ARTEMIS computer program are shown in Fig. 4 and collected in Table 4. In general, these data are consistent with the results of X-ray absorption spectroscopy, quantum chemical, and AIMD calculations previously reported in the literature (Pokrovski et al., 2009; Mei et al., 2013). In chloride-bearing fluids two Cl^- ions are the nearest neighbors of Au with $R_{Au\text{-}Cl}$ = 2.25 - 2.28 Å. Results of the present study, however, reveal some important features of Au chemistry which were not manifested previously. It follows from data of Table 4 that Au-Cl distance in the first coordination sphere weakly decreases with increasing pressure. These small systematic changes were monitored in all the studied systems. The most pronounced change in the $R_{Au\text{-}Cl}$ of 0.02 Å was observed between experiments cap118 and cap117 (the pressure increased from 2100 to 4500 bar

for fluids of identical composition). The maximum value of R_{Au-Cl} = 2.28 Å was monitored in dry chloride melt when pressure did not exceeded one bar. Therefore, one can conclude that increase of pressure induces contraction of the first coordination sphere of Au.

In all the experiments the presence of a heavy Me atom (Me = K or Cs) was observed in the second coordination sphere of Au (the contribution of Au-Me-Au path to the Fourier transform of EXAFS spectra is shown in Fig. A1). The coordination numbers and Debye-Waller parameters of cations were estimated with high uncertainty, but inclusion of Au-Me-Au path in the fits of the EXAFS spectra improved considerably the fit results in the 2.5 - 4 Å range (not corrected for phase shift) in comparison with the model without the distant-coordination-sphere cation (Table A1, Fig. A2). When it was possible to calculate the coordination number of Me atoms (N_{Me}) in the second coordination sphere of Au the N_{Me} fell within 0.2 - 0.6. In contrast to the observed contraction of the first coordination sphere of Au with increase of pressure, the opposite effect was monitored for the Me atoms in the second coordination sphere. The increase of the aqueous fluid pressure resulted in the increase of the Au-Me distance. The effect of pressure is of sharp focus in experiments cap118 (R_{Au-Me} = 3.31±0.05 Å, P = 2100 bar, d = 0.68 g·cm^{-3}) and cap117 (R_{Au-Me} = 4.14±0.03 Å, P = 4500 bar, d = 1.04 g·cm^{-3}). We note here that, despite high uncertainty, decrease of the R_{Au-Me} is of systematic character. It was observed, at a quantitative level, in all the experimental systems even though the exact change of the R_{Au-Me} as a function of *TP*-parameters can not be determined via the experimental spectra fitting.

The observed changes of the R_{Au-Me} can be explained by the effect of dielectric constant on the weakly bound distant-coordination-sphere ion. The decrease of density results in the decrease of the fluid dielectric constant which promotes electrostatic interaction of the negatively charged $AuCl_2^-$ complex and positively charged Me^+ ion. As a result, R_{Au-Me} decreases with decrease of pressure (density, dielectric constant) due to the enhancement of coulomb interaction.

3.3. Results of AIMD simulations

Simulation results are given in Table 2 (calculation parameters), Table 5 (geometry of Au species), and shown in Fig. 5. All the simulations for aqueous fluids were performed for 450 °C in order to compare the effect of the system composition on the Au-Cl complexing and the X-ray absorption spectra, and for 650 °C in the case of chloride melt. The first coordination sphere of Au comprises two chloride atoms in all the simulations but simulation F (chloride melt). In the latter case the presence of Cl^- ions at 2.6 - 3 Å induces an asymmetric shape of Cl atomic density function (Fig. 5). The distant coordination sphere of Au is composed of H_2O, Cl, and alkaline metal cations. The atomic density curves for Na, K, and Cs is of diffuse character with maxima located between 3 and 6 Å. This shape of the density curves confirms our conclusion based on the analysis of EXAFS spectra about weak electrostatic interaction of $AuCl_2^-$ with the distant-coordination-shell cations. In this case the cation does not have a definite position, but the $R_{Au\text{-}Me}$ fluctuates within ~3 - 6 Å range. The $R_{Au\text{-}Me}$ depends on the cation type and increases with increasing cation atomic weight ($R_{Au\text{-}Na}$ = 2.8 - 4.6 Å, $R_{Au\text{-}Cs}$ = 3.3 - 6 Å). The coordination number N_{Me} is not a constant but increases with increasing cationic weight and salt concentration (Table 5), which is unlike for a stable aqueous complex which has a definite composition. Computation G, which was performed for the same system composition as the computation E, but with extended atomic basis set, yielded similar results. In both calculations Cs atoms fluctuate at a distance of 3 - 6 Å with the maximum of atomic density at ~ 4 Å. Therefore, the DZVP basis set is accurate enough for AIMD investigation of hydrothermal Au complexing.

3.4. AIMD-EXAFS spectra and comparison with experimental data

EXAFS spectra simulated using atomic configurations produced by AIMD calculations are shown in Fig. A3 (chloride melt) and Fig. A4 (hydrothermal fluids). The contribution of cation in the second coordination sphere of Au to the Fourier Transform (FT) of calculated EXAFS signal increases with increasing cation atomic number and concentration, but has a significant input only on the spectrum of chloride melt (Fig. A3). In case of chloride fluids (Fig. A4) the contribution of

the distant-coordination-sphere cation calculated from the AIMD atomic configurations is underestimated relatively to the experimental spectra fitting. Nonetheless, the AIMD-EXAFS calculations enabled us lo explore the cation contribution to the EXAFS spectra using wavelet transform (WT) diagrams.

Figure 6a shows contributions of scattering atoms (Cl, O, Cs) and multiple scattering contribution Cl-Au-Cl to the WT of calculated AIMD-EXAFS spectra. The maxima of Cl contribution to the 1st coordination sphere is located at $k \sim 6$Å^{-1}, the Cl-Au-Cl multiple scattering contribution is located at $k \sim 5.5$ Å^{-1}, and the maxima of O contribution is at $k \sim 4.5$ Å^{-1} (the other local maxima of the WT of EXAFS in Fig. 6a correspond to the distant coordination sphere atoms and multiple scattering paths). The contribution of Cs is clearly seen in Fig. 6b which shows the WT of EXAFS signal of experiment cap118 – the high-temperature fluid of relatively low density (575 °C/2100 bar, $d = 0.68$ g·cm^{-3}). Here the contribution of Cs in the second coordination sphere occurs at $k \sim 9.5$ Å^{-1}/$R \sim 3$ Å. The WT of EXAFS of fluid of the same composition at higher temperature and pressure (experiment cap 117, 450 °C/4500 bar, $d = 1.04$ g·cm^{-3}) does not exhibit a notably heavy atom contribution except, probably, a small increase of the signal at $k \sim 9.7$ Å^{-1}/$R \sim$ 4.5 Å. The observed decrease of the heavy atom contribution to EXAFS signal, which takes place with increase of the fluid density, is in line with experimental EXAFS spectra fittings performed using ARTEMIS program (section 3.2, Table 4).

3.5. AIMD-XANES spectra

The Au L_3-edge HERFD-XANES spectra calculated using atomic configurations obtained by means of AIMD simulations are shown in Fig. 7. We calculated only the spectra of CsCl/NaCl/KCl melt, HCl- and CsCl-dominated fluids in order to reveal, on a quantitative level, the effect of the cation type (the lightest H^+ vs. the heaviest Cs^+) and cation concentration on the shape of the HERFD-XANES spectra. It can be seen in the figure that the WL intensity depends on the system composition. The most intense WLs correspond to systems with low salt concentration or

449 pure HCl fluid (spectra $AuCl_2Cs$ and $AuCl_2H$, correspondingly). The WL intensity of 4*m* CsCl and
450 CsCl/NaCl/KCl melt (spectra $AuCl_2Cs_4$ and melt, correspondingly) is lower. The decrease of the
451 WL intensity in salt-rich systems is similar to the one observed in our HERFD-XAS experiments
452 discussed in section 3.1. At the same time, the shift of the e.j. and the WL to lower energies in salt-
453 rich systems predicted by the simulations were not observed in the experiments. We have to note
454 that the energy positions of the spectral features in the *ab initio* calculations can be subjected to
455 substantial uncertainty.

456 The observed peculiarities of the WL intensity can be explained by the effect of cation on
457 the electronic density distribution within $AuCl_2^-$ complex. Figure 8a demonstrates that the
458 probability of finding a second-coordination-shell cation of Au has a maximum at a distance of ca.
459 4 Å at Cs-Au-Cl angle of 65°. As an alkali metal cation approaches Au the positive charge of Au
460 decreases (Fig. 8b) due to the decrease of 5*d* unoccupied DOS. This behavior of Au charge state
461 yields the WL intensity decrease. Thus, the presence of an alkali metal cation in the distant
462 coordination sphere of Au accounts for the observed decrease of the WL intensity of Au L_3-edge
463 HERFD-XANES spectra of salt-rich systems.

464

465 **3.6. Speciation and concentration of Au in natural chloride fluids and melts**

466 Salinity (chlorinity) of natural hydrothermal fluids varies in wide limits from almost dry
467 melts to diluted aqueous solutions. Results of our study demonstrate that, independently of fluid
468 chemistry (cation type and chloride salt concentration), $AuCl_2^-$ is the dominant Au species in fluids
469 of moderate to high density. The Au dissolution in aqueous fluids can be described by the reaction,

470 $$Au_{(cr)} + HCl°_{(aq)} + Cl^- = AuCl_2^- + 0.5\ H_{2(g)} \quad , \quad (4)$$

471 or, involving the proton activity (or $pH = -\log a(H^+)$),

472 $$Au_{(cr)} + H^+ + 2\ Cl^- = AuCl_2^- + 0.5\ H_{2(g)} \quad , \quad (5)$$

473 or, using oxygen as a reactant which acts as an oxidizing agent,

474 $$Au_{(cr)} + HCl°_{(aq)} + Cl^- + 0.25\ O_{2(g)} = AuCl_2^- + 0.5\ H_2O \quad . \quad (6)$$

Similar reaction can be written for Au dissolution in dry chloride melt,

$$Au_{(cr)} + 2\ Cl^- + 0.25\ O_{2(g)} = AuCl_2^- + 0.5\ O^{2-} \quad , \quad (7)$$

or, in terms of neutral species,

$$Au_{(cr)} + 2\ NaCl + 0.25\ O_{2(g)} = NaAuCl_2 + 0.5\ Na_2O \quad . \quad (8)$$

These reactions imply that the solubility (concentration) of Au is governed by (i) the oxygen fugacity, (ii) the fluid acidity, and, (iii) the chloride concentration. It follows from Eq. (4-8) that the dissolved Au concentration in equilibrium with native gold increases proportionally to the first power of fluid acidity, the second power of chloride salt concentration, and decreases as a square root of hydrogen fugacity (or increases proportionally to $f(O_2)^{0.25}$). Predominance field of $AuCl_2^-$ falls within acidic range of pH. In sulfide-rich fluids the Au solubility is controlled by hydrosulfide complex $Au(HS)_2^-$ in the pH range from weakly acidic to alkaline, even in the presence of chlorides (e.g., Renders and Seward, 1989; Shenberger and Barnes, 1989; Benning and Seward, 1996; Stefánsson and Seward, 2003; Barnes, 2015; Trigub et al., 2017, see also references cited in these papers), or by hydroxide complex Au(OH)° at high (> 400 °C) temperatures (Zotov et al., 1985; Stefánsson and Seward, 2003). The dissolved Au concentration in dry chloride melt is mostly controlled by the oxygen fugacity and increases as a linear function of $f(O_2)^{0.25}$ (Eq. 7, 8).

Results of our spectroscopic experiments revealed the difference between the first and second coordination spheres of Au complexes. The Cl^- ions in the nearest coordination sphere of Au are bonded to the central atom via the formation of strong chemical bond whose nature can be described in terms of interaction between the metal and ligand atomic orbitals with the formation of molecular orbitals (cf. Figgs and Fitchman, 2000). In contrast, cations (H^+, Na^+, K^+, Cs^+ in the case of the present study) are weakly bonded to the negatively charged $AuCl_2^-$ complex in the distant coordination sphere of Au mostly via the electrostatic interaction. The difference in the chemical bond properties is clearly demonstrated by the contrasting behavior of the atoms in the nearest and distant coordination spheres depending on the experimental *TP*-parameters. Increasing pressure results in weak contraction of the first coordination sphere of Au, whereas conjugated increase of

501 the dielectric constant of hydrothermal fluid causes expansion of the distant coordination sphere
502 composed of alkali metal cations. The number of cations in the distant coordination sphere of Au
503 also depends upon pressure, cation type, and salt concentration. From the point of view of
504 thermodynamics this means that the dissolution of Au can be explicitly described by the equilibrium
505 constants of chemical reactions which involve the formation of $AuCl_2^-$ (Eq. 4-8), taking into
506 account the influence of weak outer sphere coulomb interactions via the activity coefficients. This
507 approach is valid for fluids with density of $d > 0.5$ g·cm^{-3}. In low-density fluids ($d < 0.3$ g·cm^{-3}),
508 where interaction between charged species becomes much more pronounced and neutral species
509 predominate, formation of ionic associates of the type of $MeAuCl_2°$ and $HAuCl_2°$ is hampered by
510 the change of predominant Au complex from charged $AuCl_2^-$ to neutral AuCl°. The same
511 conclusion might be done with regard to other 1st group *d*-elements (Cu, Ag) which form stable
512 chloride complexes of similar composition. However, determination of composition and stability of
513 chloride complexes of these metals can only be done via accurate solubility measurements.

514 The Au solubililties monitored in the present study are in close agreement with
515 thermodynamic model of Akinfiev and Zotov (2010), which is based on the consideration of $AuCl_2^-$
516 complex. We note, however, that there is still a problem of disagreement between the values of
517 $AuCl_2^-$ stability constants reported in the key studies on hydrothermal Au-Cl complexing of Zotov
518 et al. (1991) and Stefánsson and Seward (2003). The Au solubility constants obtained in Zotov et al.
519 (1991) are more than one log unit higher than those determined in Stefánsson and Seward (2003)
520 for similar *TP*-parameters. The reason of this deviation is unclear. This problem can be resolved by
521 additional measurements of Au solubility with rigorous in situ control of the most important
522 physicochemical parameters (e.g., $f(H_2)$), and in situ experimental solution sampling. This is an
523 ongoing study in our laboratory.

524

525 **4. CONCLUSIONS**

In the present study we recorded Au L_3-edge X-ray absorption spectra of aqueous chloride-bearing fluids at temperatures 350 – 575 °C and pressures up to 4500 bar. The composition of the experimental fluids varied from HCl – dominated solutions to concentrated KCl and CsCl brines. X-ray absorption spectra of dry CsCl/NaCl/KCl melt were recorded at 650 °C. Interpretation of EXAFS spectra showed that, independently of the experimental fluid composition, $AuCl_2^-$ complex dominates the dissolved Au speciation. The distance between Au and the nearest-neighbor Cl atoms varies between 2.25 – 2.28 Å. This interatomic distance is pressure-dependent and decreases with increasing pressure from 2.28 Å (dry melt) to 2.25 Å (7.3*m* HCl/4.2*m* CsCl fluid at 4500 bar). The outer coordination sphere of Au is composed of cations located at a distance of 3.3 – 4.1 Å. In contrast to the inner coordination sphere, the outer coordination shell expands with increasing the fluid pressure (dielectric constant). The number of cations located in the outer coordination sphere increases with increasing cation atomic number and concentration. Such a contrasting behavior of atoms located in the nearest and distant coordination spheres of Au reveals the difference in the nature of the chemical bonds. Chloride ions are connected to Au by means of strong chemical bonding, whereas weak coulomb interactions between $AuCl_2^-$ and cations are responsible for the formation of the disordered distant coordination sphere. The presence of cations in the distant coordination sphere of Au is confirmed by the change of the shape of Au L_3-edge HERFD-XANES spectra in salt-rich brine and dry melt with respect to the HCl-dominated fluid. The results of our study imply that the Au solubility in hydrothermal fluids in the wide range of *TP*-conditions and chlorides concentration can be described in terms of the formation of $AuCl_2^-$ complex using an appropriate model for the activity coefficients.

Acknowledgements

The authors acknowledge the ESRF for the beamtime allocation under proposals 20-01-782 (BM20 beamline) and ES-360 (ID26 beamline). We thank Hugo Vitoux for technical support during the in-situ experiment with a micro-tomo furnace at ID26, and Joerg Exner for technical

552 support at BM20. The authors are grateful to Alexander Zotov and Nikolai Akinfiev for useful
553 discussions during the manuscript preparation. Pavel Selivanov is acknowledged for preparation of
554 capillaries and technical assistance during the synchrotron experiments. We thank Max Wilke,
555 Elena Bazarkina, and Laurent Truche for providing us with silica glass capillaries. The results of
556 this work were obtained using the computational resources of MCC NRC "Kurchatov Institute"
557 (http://computing.kiae.ru/). Chemical analyses were carried out at the "IGEM-Analytica" Center for
558 collective use. This study was supported by the Russian Science Foundation grant No. 17-17-01220
559 (spectroscopic experiment and interpretation, AIMD calculations) and Basis theme RAS No. 72-7
560 (thermodynamic speciation calculations). The work of DACh is supported by the program 211 of
561 the Russian Federation Government, agreement No. 02.A03.21.0006 and by the Russian
562 Government Program of Competitive Growth of Kazan Federal University.

REFERENCES

Akinfiev N. N. and Zotov A. V. (2010) Thermodynamic description of aqueous species in the system Cu-Ag-Au-S-O-H at temperatures of 0-600°C and pressures of 1-3000 bar. *Geochem. Int.* **48,** 714-720.

Ankudinov A. L., Ravel B., Rehr J. J. and Conradson S. D. (1998) Real space multiple scattering calculation of XANES. *Phys. Rev. B* **58,** 7565.

Archibald S. M., Migdisov A. A. and Williams-Jones A. E. (2001) The stability of Au-chloride complexes in water vapor at elevated temperatures and pressures. *Geochim. Cosmochim. Acta* **65,** 4413–4423.

Bach R. W., Friedrichs H. A. and Rau H (1977) *P-V-T* relations for HCl-H_2O mixtures up to 500 °C and 1500 bars. *High Temp. High Press.* **9,** 305-312.

Bader R. F. W. (1990) *Atoms in molecules: a quantum theory.* Oxford University Press: Oxford, U.K.

Bader R. F. W. (1991) A Quantum theory of molecular structure and its applications. *Chem. Rev.* **91,** 893−928.

Ballhaus C. G. and Stumpfl E. F. (1986) Sulfide and platinum mineralization in the Merensky Reef: evidence from hydrous silicates and fluid inclusions. *Contrib. Mineral. Petrol.* **94,** 193-204.

Barnes H. L. (2015) Hydrothermal processes. *Geochem. Persp.* **4,** 1-93.

Bellet D., Gorges B., Dallery A., Bernard P., Pereiro E. and Baruchel J. (2003) A 1300 K furnace for in situ X-ray microtomography. *J. Appl. Cryst.* **36,** 366-367.

Benning L. G and Seward T. M. (1996) Hydrosulphide complexing of Au (I) in hydrothermal solutions from 150–400°C and 500–1500 bar**.** *Geochim. Cosmochim. Acta* **60,** 1849-1871.

Berendsen H. J. C., van der Spoel D. and van Drunen R. (1995) GROMACS: A message-passing parallel molecular dynamics implementation. *Comp. Phys. Comm.* **91,** 43-56. http://www.gromacs.org/.

Bortnikov N. S., Simonov V. A. and Bogdanov Yu. A. (2004) Fluid inclusions in minerals from modern sulfide edifices: physicochemical conditions of formation and evolution of fluids. *Geology of Ore Deposits* **46**(1), 64-75.

Bortnikov N. S., Simonov V. A., Amplieva E. E. and Borovikov A. A. (2014) Anomalously high concentrations of metals in fluid of the Semenov modern hydrothermal system (Mid-Atlantic Ridge, 1331′ N): LA–ICP–MS study of fluid inclusions in minerals. *Doklady Earth Sciences* **456**(2), 714-719.

Bunău O. and Joly Y. (2009) Self-consistent aspects of X-ray absorption calculations. *J. Phys. Cond. Mat.* **21,** 345501.

Chaplygin I. V., Mozgova N. N., Mokhov A. V., Koporulina E. V., Bernhardt H.-J., Bryzgalov I. A. (2007) Minerals of the system ZnS–CdS from fumaroles of the Kudriavy volcano, Iturup Island, Kuriles, Russia. *Can. Minaral.* **45,** 709-722.

Chaplygin I., Yudovskaya M., Vergasova L. and Mokhov A. (2015) Native gold from volcanic gases at Tolbachik 1975-76 and 2012-13 Fissure Eruptions, Kamchatka. *J. Volcanol. Geotherm. Res.* **307,** 200-209.

Chareev D. A., Volkova O. S., Geringer N. V., Koshelev A. V., Nekrasov A. N., Osadchii V. O., Osadchii E.G., Filimonova O. N. (2016) Synthesis of chalcogenide and pnictide crystals in salt melts using a steady-state temperature gradient. *Crystallography Reports*, **61**(4), 682-691.

Chou I-M. (2012) Optical cells with fused silica windows for the study of geological fluids. In *Applications of Raman Spectroscopy to Earth Sciences and Cultural Heritage* (eds. J. Dubessy, M.-C. Gaumont and F. Rull). EMU Notes in Mineralogy, V. 12, London, pp. 227-248.

Chou I-M., Song Y. and Burruss R. C. (2008) A new method for synthesizing fluid inclusions in fused silica capillaries containing organic and inorganic material. *Geochim. Cosmochim. Acta* **72,** 5217-5231.

Ding J. (2010) The pH determination of palaeofluids: experimental and thermodynamic approach. Ph. D. thesis, Université Henri Poincaré, Nancy.

Douville E., Charlou J. L., Oelkers E. H., Bienvenu P., Jove Colon C. F., Donval J. P., Fouquet Y., Prieur D. and Appriou P. (2002) The Rainbow vent fluids (36°4', MAR): the influence of ultramafic rocks and phase separation on trace metal content in Mid-Atlantic Ridge hydrothermal fluids. *Chem. Geol.* **184,** 37-48.

Driesner T. (2007) The system H_2O-NaCl. II. Correlations for molar volume, enthalpy, and isobaric heat capacity from 0 to 1000 °C, 1 to 5000 bar, and 0 to 1 X_{NaCl}. *Geochim. Cosmochim. Acta* **71,** 4902-4919.

Driesner T. and Heinrich C. A. (2007) The system H_2O-NaCl. I. Correlation formulae for phase relations in temperature-pressure-composition space from 0 to 1000 °C, 0 to 5000 bar, and 0 to 1 X_{NaCl}. *Geochim. Cosmochim. Acta* **71,** 4880-4901.

Figgs B. N. and Hitchman M. A. (2000) *Ligand field theory and its applications.* Wiley-YCH.

Frank M. R., Candela P. A., Piccoli P. M. and Glascock M. D. (2002) Gold solubility, speciation, and partitioning as a function of HCl in brine-silicate melt-metallic gold system at 800°C and 100 MPa. *Geochim. Cosmochim. Acta* **66,** 3719-3732.

Frisch M. J., Trucks G. W., Schlegel H. B., Scuseria G. E., Robb M. A., Cheeseman J. R., Scalmani G., Barone V., Petersson G. A., Nakatsuji H., Li X., Caricato M., Marenich A., Bloino J., Janesko B. G., Gomperts R., Mennucci B., Hratchian H. P., Ortiz J. V., Izmaylov A. F., Sonnenberg J. L., Williams-Young D., Ding F., Lipparini F., Egidi F., Goings J., Peng B., Petrone A., Henderson T., Ranasinghe D., Zakrzewski V. G., Gao J., Rega N., Zheng G., Liang W., Hada M., Ehara M., Toyota K., Fukuda R., Hasegawa J., Ishida M., Nakajima T., Honda Y., Kitao O., Nakai

637 H., Vreven T., Throssell K., Montgomery Jr. J. A., Peralta J. E., Ogliaro F., Bearpark M., Heyd J.
638 J., Brothers E., Kudin K. N., Staroverov V. N., Keith T., Kobayashi R., Normand J., Raghavachari
639 K., Rendell A., Burant J. C., Iyengar S. S., Tomasi J., Cossi M., Millam J. M., Klene M., Adamo C.,
640 Cammi R., Ochterski J. W., Martin R. L., Morokuma K., Farkas O., Foresman J. B. and Fox D.J.
641 (2016) Gaussian 09. Gaussian Inc., Wallingford CT.

642 Fullam H. T. (1971) *Physical property measurements on cesium chloride and cesium*
643 *chloride – alkali metal chloride systems.* Atlantic Richfield Hanford Company.

644 Funke H., Chukalina M. and Scheinost A. (2007) A new FEFF-based wavelet for EXAFS
645 data analysis. *J. Synchr. Radiation* **14**, 426–432.

646 Gauthier C., Sole V. A., Signorato R., Goulon J. and Moguiline E. (1999) The ESRF
647 beamline ID26: X-ray absorption on ultra dilute sample. *J. Synchr. Radiation* **6,** 164-166.

648 Giannozzi P., Baroni S., Bonini N., Calandra M., Car R., Cavazzoni C., Ceresoli D., Chiarotti
649 G. L., Cococcioni M., Dabo I., Corso A. D., de Gironcoli S., Fabris S., Fratesi G., Gebauer R.,
650 Gerstmann U., Gougoussis C., Kokalj A., Lazzeri M., Martin-Samos L., Marzari N., Mauri F.,
651 Mazzarello R., Paolini S., Pasquarello A., Paulatto L., Sbraccia C., Scandolo S., Sclauzero G.,
652 Seitsonen A. P., Smogunov A., Umari P. and Wentzcovitch R. M. (2009) QUANTUM ESPRESSO:
653 a modular and open-source software project for quantum simulations of materials. *J. Phys. Cond.*
654 *Matt.* **21,** 395502.

655 Glatzel P. and Bergman U. (2005) High resolution 1s core hole X-ray spectroscopy in 3d
656 transition metal complexes - electronic and structural information. *Coord. Chem. Rev*. **249,** 65-95.

657 Goedecker S., Teter M. and Hutter J. (1996) Separable dual-space Gaussian
658 pseudopotentials. *Phys. Rev. B* **54,** 1703–1710.

659 Gregory M. J. (2017) A fluid inclusion and stable isotope study of the Pebble porphyry
660 copper-gold-molybdenum deposit, Alaska. *Ore Geol. Rev.* **80**, 1279-1303.

661 Guda S. A., Guda A. A., Soldatov M. A., Lomachenko K. A., Bugaev A. L., Lamberti C.,
662 Gawelda W., Bressler C., Smolentsev G., Soldatov A. V. and Joly Y. (2015) Optimized finite

663 difference method for the full-potential XANES simulations: application to molecular adsorption
664 geometries in MOFs and metal-ligand intersystem crossing transients. *J. Chem. Theory Comp.* **11**,
665 4512-4521.

666 Guo H., Audétat A. and Dolejš D. (2018) Solubility of gold in oxidized, sulfur-bearing
667 fluids at 500–850 °C and 200–230 MPa: A synthetic fluid inclusion study. *Geochim. Cosmochim.*
668 *Acta* **222,** 655-670.

669 Hanley J. J., Mungall J. E., Pettke T., Spooner E. T. C. and Bray C. J. (2008) Fluid and
670 halide melt inclusions of magmatic origin in the ultramafic and lower banded series, Stillwater
671 complex, Montana, USA. *J. Petrol.* **49,** 1133-1160.

672 Hartwigsen C., Goedecker S. and Hutter J. (1998) Relativistic separable dual-space
673 Gaussian pseudopotentials from H to Rn. *Phys. Rev. B* **58,** 3641–3662.

674 Heinrich C. A., Driesner T., Stefansson A. and Seward T. M. (2004) Magmatic vapor
675 contraction and the transport of gold from the porphyry environment to epithermal ore deposits.
676 *Geology* **32,** 761-764.

677 Joly Y. (2001) X-ray absorption near-edge structure calculations beyond the muffin-tin
678 approximation. *Phys. Rev. B* **63,** 125120-125129.

679 Karpukhina V. S., Naumov V. B. and Vikent'ev I. V. (2013) Genesis of massive sulfide
680 deposits in the Verkhneural'sk Ore District, the South Urals, Russia: Evidence for magmatic
681 contribution of metals and fluids. *Geology of Ore Deposits* **55**(2), 125-144.

682 Krack M. (2005) Pseudopotentials for H to Kr optimized for gradient-corrected exchange-
683 correlation functionals. *Theor. Chem. Acc.* **114,** 145–152.

684 Kvashnina K. O. and Scheinost A. C. (2016) A Johann-type X-ray emission spectrometer at
685 the Rossendorf Beamline. *J. Synch. Radiation* **23,** 836–841.

686 Large R. R. (1977) Chemical evolution and zonation of massive sulfide deposits in volcanic
687 terrains. *Econ. Geol.* **72,** 549-572.

Lippert G., Hutter J. and Parrinello M. (1997) A hybrid Gaussian and plane wave density functional scheme. *Mol. Phys.* **92,** 477–487.

Matsushita N, Ahsbahs H., Hafner S. S. and Kojima N. (1998) Crystal structure of mixed valence gold compound, $Cs_2Au(I)Au(III)Cl_6$ up to 18 GPa. *Rev. High Pressure Sci. Technol.* **7,** 329-331.

Mei Y., Liu W., Sherman D. M. and Brugger J. (2014) Metal complexing and ion hydration in low density hydrothermal fluids: ab initio molecular dynamics simulation of Cu(I) and Au(I) in chloride solutions (25-1000 °C, 1-5000 bar). *Geochim. Cosmochim. Acta* **131,** 196-212.

Miceli G., de Gironcoli S. and Pasquarello A. (2015) Isobaric first-principles molecular dynamics of liquid water with nonlocal van der Waals interactions. *J. Chem. Phys.* **142**, 034501.

Nosé S. (1984a) A molecular dynamics method for simulations in the canonical ensemble. *Mol. Phys.* **52,** 255-268.

Nosé S. (1984b) A unified formulation of the constant temperature molecular dynamics methods. *J. Chem. Phys.* **81,** 511.

Otero-de-la-Roza A., Blanco M. A., Martín Pendás A. and Luaña V. (2009) Critic: a new program for the topological analysis of solid-state electron densities. *Comp. Phys. Com.* **180,** 157-166.

Otero-de-la-Roza A., Johnson E. R. and Luaña V. (2014) Critic2: A program for real-space analysis of quantum chemical interactions in solids. *Com. Phys. Com.* **185,** 1007-1018.

Penfold T. J., Tavernelli I., Milne C. J., Reinhard M., El Nahhas A., Abela R., Rothlisberger U. and Chergui M. (2013) A wavelet analysis for the X-ray absorption spectra of molecules. *J. Chem. Phys.* **138,** 014104.

Perdew P., Burke K. and Ernzerhof M. (1996) Generalized gradient approximation made simple. *Phys. Rev. Lett.* **77,** 3865-3868.

709 Pokrovski G. S., Tagirov B. R., Schott J, Bazarkina E. F., Hazemann J.-L. and Proux O.
710 (2009) An in situ X-ray absorption spectroscopy study of gold-chloride complexing in hydrothermal
711 fluids. *Chem. Geol*. **259,** 17-29.
712 Ravel B. and Newville M. (2005) ATHENA, ARTEMIS, HEPHAESTUS: data analysis for
713 X-ray absorption spectroscopy using IFEFFIT. *J. Synchr. Radiation* **12,** 537-541.
714 Renders R. J. and Seward T. M. (1989) The stability of hydrosulphido- and sulphido-
715 complexes of Au(I) and Ag(I) at 25°C. *Geochim. Cosmochim. Acta* **53,** 245-253.
716 Sabatini R., Gorni T. and de Gironcoli S. (2013) Nonlocal van der Waals density functional
717 made simple and efficient. *Phys. Rev. B: Condens. Matter Mater. Phys.* **87**, 041108.
718 Schmidt K., Garbe-Schönberg D., Koschinky A., Strauss H., Jost C.L., Kleven V. and
719 Königer P. (2011) Fluid elemental and stable isotope composition of the Nibelungen hydrothermal
720 field (8°18′ S, Mid-Atlantic Ridge): Constraints on fluid–rock interaction in heterogeneous
721 lithosphere. *Chem. Geol.* **280,** 1–18.
722 Seward T. M., Williams-Jones A. E. and Migdisov A. A. (2014) The chemistry of metal
723 transport and deposition by ore-forming hydrothermal fluids. In *Treatise on Geochemistry* (eds. K.
724 Turekian and H. Holland). 2nd edition. V. 13. Elsevier, pp. 29-57.
725 Shenberger D. M. and Barnes H. L. (1989) Solubility of gold in aqueous sulfide solutions
726 from 150 to 350 °C. *Geochim. Cosmochim. Acta* **53,** 269-278.
727 Shmulovich K. I. and Churakov S. V. (1998) Natural fluid phases at high temperatures and
728 low pressures. *J. Geochem. Expl.* **62,** 183-191.
729 Shmulovich K. I., Bukhtiyarov P. G. and Persikov E. S. (2016) Gold transport during
730 magmatic degassing: model experiments. *Geochem. Int.* **54**(11), 979-988.
731 Sillitoe R. H. (2010) Porphyry copper systems. *Econ. Geol*. **105,** 3-41.
732 Simonov V. A., Kovyazin S. V., Terenya E. O., Maslennikov V. V., Zaykov V. V. and
733 Maslennikova S. P. (2006). Physicochemical parameters of magmatic and hydrothermal processes

734 at the Yaman-Kasy massive sulfide deposit, the Southern Urals. *Geology of Ore Deposits* **48**(5),
735 369-383.
736 Sluzhenikin S. F. and Mokhov A. V. (2015) Gold and silver in PGE-Cu-Ni and PGE ores of
737 the Norils'k deposits, Russia. *Miner. Deposita* **50,** 465-492.
738 Stefánsson A. and Seward T. M. (2003) The stability of chloridogold(I) complexes in
739 aqueous solutions from 300 to 600°C and from 500 to 1800 bar. *Geochim. Cosmochim. Acta* **67,**
740 4459–4576.
741 Stefánsson A. and Seward T. M. (2004) Gold(I) complexing in aqueous sulphide solutions
742 to 500°C at 500 bar. *Geochim. Cosmochim. Acta* **68,** 4121-4143.
743 Tagirov B. R., Zotov A. V. and Akinfiev N. N. (1997) Experimental study of dissociation of
744 HCl from 350 to 500^{o}C and from 500 to 2500 bars: Thermodynamic properties of $HCl_{(aq)}$. *Geochim.*
745 *Cosmochim. Acta* **61,** 4267-4280.
746 Timoshenko J. and Kuzmin A. (2009) Wavelet data analysis of EXAFS spectra. *Comput.*
747 *Phys. Comm.* **180,** 920–925.
748 Trigub A. L., Tagirov B. R., Kvashnina K. O., Chareev D. A., Nickolsky M. S., Shiryaev A.
749 A., Baranova N. N., Kovalchuk E. V. and Mokhov A. V. (2017a) X-ray spectroscopy study of the
750 chemical state of "invisible" Au in synthetic minerals in the Fe-As-S system. *Am. Mineral.* **102,**
751 1057-1065.
752 Trigub A. L., Tagirov B. R., Kvashnina K. O., Lafuerza S., Filimonova O. N. and Nickolsky
753 M. S. (2017b) Experimental determination of gold speciation in sulfide-rich hydrothermal fluids
754 under a wide range of redox conditions. *Chem. Geol.* **471**, 52-64.
755 VandeVondele J., Krack M., Mohamed F., Parrinello M., Chassaing T. and Hutter J. (2005)
756 Quickstep: fast and accurate density functional calculations using a mixed Gaussian and plane
757 waves approach. *Comput. Phys. Comm.* **167,** 103-128. http://www.cp2k.org.

Vikent'ev I. V., Borisova A. Yu., Karpukhina V. S., Naumov V. B. and Ryabchikov I. D. (2012) Direct data on the ore potential of acid magmas of the Uzel'ginskoe ore field (Southern Urals, Russia). *Doklady Earth Sciences* **443**(1), 401–405.

Vikent'ev I. V., Karpukhina V. S., Nosik L. P. and Eremin N. I. (2009) Formation conditions of the Tash-Yar zinc massive sulfide deposit, Southern Urals. *Doklady Earth Sciences* **429**(8), 1241–1244.

Vydrov O. A. and Van Voorhis T. (2009) Nonlocal van der Waals density functional made simple. *Phys. Rev. Lett.* **103**, 63004−63007.

Yudovskaya M. A., Distler V. V., Chaplygin I. V., Trubkin N. V. and Gorbacheva S. A. (2006) Gaseous transport and deposition of gold in magmatic fluid: evidence from the active Kudryavy volcano, Kurile Islands. *Miner. Deposita* **40,** 828-848.

Zabinsky S. I., Rehr J. J., Ankudinov A., Albers R. C. and Eller M. J. (1995) Multiple-scattering calculations of X-ray-absorption spectra. *Phys. Rev. B* **52,** 2995-3009.

Zajacz Z., Seo J. H., Candela P. A., Piccoli P. M., Heinrich C. A. and Guillong M. (2010) Alkali metals control the release of gold from volatile-rich magmas. *Earth Plan. Sci. Lett.* **297,** 50-56.

Zhitova L. M., Kinnaird J. A., Gora M. P. and Shevko E. P. (2016) Magmatogene fluids of metal-bearing reefs in the Bushveld Complex, South Africa: based on research data on fluid inclusions in quartz. *Geology of Ore Deposits* **58**(1), 58-80.

Zotov A. V., Baranova N. N., Dar'yina T. G., Bannykh L. N. and Kolotov V. P. (1985) The stability of $AuOH°_{sol}$ in water at 300 – 500 °C and 500 – 1500 atm. *Geochem. Int.* **22**(5)**,** 156-161.

Zotov A. V. and Baranova N. N (1989) Thermodynamic properties of the aurochloride solute complex $AuCl_2^-$ at temperatures of 350-500°C and pressures of 500-1500 bars. *Sciences Géologiques, Bull.* **42**(4), 335-342.

Zotov A. V., Baranova N. N., Dar'yina T. G. and Bannykh L. M. (1989) Gold (I) complexing in the KCl-HCl-H_2O system at 450°C. *Geochem. Int.* **26**(11)**,** 66-75.

Zotov A. V., Baranova N. N., Dar'yina T. G. and Bannykh L. M. (1991) The solubility of gold in aqueous chloride fluids at 350-500 °C and 500-1500 atm: Thermodynamic parameters of $AuCl_2^-{}_{(sol)}$ up to 750°C and 500 atm. *Geochem. Int.* **28**(2)**,** 63-71.

Zotov A. V., Kudrin A. V., Levin K. A., Shikina N. D. and Var'yash L. N. (1995) Experimental studies of the solubility and complexing of selected ore elements (Au, Ag, Cu, Mo, As, Sb, Hg) in aqueous solutions. In *Fluids in the crust. Equilibrium and transport properties* (eds. K. I. Shmulovich, B. W. D. Yardley and G. G. Gonchar). Chapman & Hall. pp. 95-137.

Zotov A. V., Tagirov B. R., Koroleva L. A. and Volchenkova V. A. (2017) Experimental modeling of Au and Pt coupled transport by chloride hydrothermal fluids at 350-450 °C and 500-1000 bar. *Geology of Ore Deposits* **49**(5), 421-429.

Table

Table 1. Compositions of experimental systems, experimental Au solubilities, and equilibrium concentrations of aqueous species calculated using thermodynamic data available in the literature: $AuCl_2^-$ - Akinfiev and Zotov (2010), CsCl° - Sverjensky et al. (1997), HCl° - Tagirov et al. (1997), other aqueous species, H_2O, and $Au_{(cr)}$ – SUPCRT92 (Johnson et al., 1992).

Capillary No.	28	30	110	110	117	118	122	122	122	122
Solute Concentr.	3.8*m*HCl/ 0.02 *m*NaCl/ 0.5*m*H_2SO_4/ 0.5*m* H_2SO_3	3.4*m*NaCl/ 0.7*m*H_2SO_4/ 0.6*m* H_2SO_3	3.8*m*HCl/ 0.57*m*KCl/ 0.03*m*$K_2S_2O_8$	3.8*m*HCl/ 0.57*m*KCl/ 0.03*m*$K_2S_2O_8$	7.3*m*HCl/ 4.2*m*CsCl/ 0.56*m*H_2SO_4/ 0.12*m*Na_2SO_3	7.3*m*HCl/ 4.2*m*CsCl/ 0.56*m*H_2SO_4/ 0.12*m*Na_2SO_3	3.8*m*HCl/ 7.2*m*KCl/ 0.4*m*$K_2S_2O_8$	3.8*m*HCl/ 7.2*m*KCl/ 0.4*m*$K_2S_2O_8$	3.8*m*HCl/ 7.2*m*KCl/ 0.4*m*$K_2S_2O_8$	3.8*m*HCl/ 7.2*m*KCl/ 0.4*m*$K_2S_2O_8$
d, g·cm^{-3}	0.53	0.67	0.71	0.71	1.04	0.68	0.96	0.96	0.96	0.96
t, °C/ ***P***, bar	485 °C/ 600 bar	485 °C/ 700 bar	400 °C/ 850 bar	450 °C/ 2100 bar	450 °C/ 4500 bar	575 C°/ 2100 bar	350 °C/ 150 bar	400 °C/ 500 bar	450 °C/ 1100 bar	525 °C/ 1900 bar
Calculated concentrations, mol·(kg H_2O)$^{-1}$										
H^+	5.73E-01	1.43E-02	4.43E-01	4.55E-01	2.21E+00	6.83E-02	3.01E-01	1.89E-01	1.04E-01	3.52E-02
OH^-	1.03E-10	7.10E-09	2.72E-10	8.84E-10	1.44E-09	5.92E-09	1.93E-10	9.86E-10	2.87E-09	1.53E-08
O_2	5.33E-10	1.62E-14	9.74E-19	1.05E-17	1.11E-19	4.37E-13	1.43E-16	6.73E-16	2.89E-15	1.48E-13
H_2	3.48E-09	2.62E-07	8.69E-09	8.01E-08	2.91E-07	3.07E-06	1.53E-11	6.29E-10	1.10E-08	2.25E-07
HSO_3^-	8.89E-09	1.73E-06	1.90E-08	7.52E-08	1.40E-06	9.07E-07	8.91E-10	2.07E-08	2.34E-07	1.83E-06
HSO_4^-	3.94E-01	6.69E-01	4.04E-02	2.55E-02	9.33E-02	3.81E-02	7.43E-01	7.70E-01	7.47E-01	6.00E-01
SO_2°	5.82E-01	6.15E-01	5.62E-03	2.04E-02	2.52E-01	6.27E-01	1.09E-04	2.91E-03	2.77E-02	1.86E-01
SO_4^{2-}	8.30E-06	5.27E-04	8.20E-07	3.33E-07	1.24E-06	7.77E-07	1.18E-04	2.06E-04	1.13E-04	8.59E-05
H_2SO_4°	1.20E-02	8.74E-04	1.39E-02	1.40E-02	3.30E-01	1.17E-03	5.63E-02	2.70E-02	2.42E-02	8.12E-03
Cl^-	1.79E-02	3.15E-01	6.96E-01	7.55E-01	3.07E+00	6.03E-01	1.61E+00	1.93E+00	1.91E+00	1.75E+00
HCl°	3.40E+00	6.11E-01	3.27E+00	3.21E+00	4.63E+00	5.87E+00	2.64E+00	2.77E+00	2.79E+00	2.38E+00
Na^+	1.49E-02	1.01E+00			1.27E-01	9.45E-02				
NaCl°	4.89E-03	2.35E+00			1.11E-01	1.41E-01				
K^+			3.65E-01	4.27E-01			2.85E+00	3.32E+00	3.40E+00	3.49E+00
KCl°			2.65E-01	2.03E-01			5.15E+00	4.68E+00	4.59E+00	4.46E+00
Cs^+					1.09E+00	1.50E+00				
CsCl°					3.08E+00	2.62E+00				
$AuCl_2^-$	1.76E-01	4.39E-02	7.12E-02	1.01E-01	2.65E-01	1.02E+00	8.00E-01	8.06E-01	8.55E-01	1.17
$Au_{exp.}$ [a]	n/d	n/d	3E-02	5E-02	2E-01	7E-01	2E-01	2E-01	2E-01	2E-01
I [b]	0.588	1.029	0.808	0.881	3.426	1.66	3.153	3.507	3.507	3.522
pH	1.386	2.864	0.881	0.797	0.154	1.87	1.366	1.586	1.753	2.19
Eh	0.34	-0.039	0.28	0.235	0.255	0.017	0.378	0.279	0.186	0.042

[a] dissolved Au concentration determined from the amplitude of the absorption edge height of Au L_3-edge transmission spectra, estimated uncertainty ±0.3 log units; [b] ionic strength.

Table 2. Results of *ab initio* molecular dynamics (AIMD) simulations performed for systems containing Au complexes of different compositions. Uncertainties correspond to the standard deviations.

AIMD calculation	Composition of simulation box	Box size, Å	Starting Au species[a]	*T*,K	Density ρ, g/cm^3 (without Au)	Density ρ, g/cm^3 (with Au)	Simula- tion time, ps
A	Au^+, H^+, $2Cl^-$, $55H_2O$	14.7	$Au(Cl)_2^-$	722 (46)	0.55	0.65	23
B	Au^+, Na^+, $2Cl^-$, $55H_2O$	14.7	$Au(Cl)_2^-$	722 (45)	0.56	0.67	23
C	Au^+, K^+, $2Cl^-$, $55H_2O$	14.7	$Au(Cl)_2^-$	722 (45)	0.57	0.67	25
D	Au^+, Cs^+, $2Cl^-$, $55H_2O$	14.7	$Au(Cl)_2^-$	722 (46)	0.62	0.72	23
E	Au^+, $4Cs^+$, $5Cl^-$, $55H_2O$	14.7	$Au(Cl)_2^-$	722 (48)	0.83	0.98	24
F	Au^+, $48Cs^+$, $32Na^+$, $27K^+$, $5Cl^-$,	16.3		923 (53)	2.13	2.17	15
G	Au^+, $4Cs^+$, $5Cl^-$, $55H_2O$	14.7	$Au(Cl)_2^-$	723 (49)	0.83	0.98	15

[a] starting system configurations were prepared using GROMACS software and included the Au complexes of indicated composition (see section 2.4 for calculation details). Starting geometry for F calculation was prepared using CsCl crystal lattice by substituting Cs atoms by Au, Na and K atoms, and correction of lattice constant to get the specified density.

Table 3. Position of edge jump (e.j.), white line (WL), and the next to WL feature (B) of Au L_3-edge HERFD- and TFY-XANES spectra (as determined by IFEFFIT program). Uncertainty of the energy values is ±0.5 eV.

Experimental system	Feature	Position, eV
HERFD-XANES (± 0.2 eV)		
cap 5407 **Melt** CsCl/NaCl/KCl ***t*** = 650 °C 45.5at.%/30 at%/24.5 at%	e.j. WL B ΔB-WL[a]	11919.5 11921.0 11930.8 9.8
cap 28 ***t*** = 485 °C, ***P*** = 600 bar ***d*** = 0.53 g·cm^{-} 3.8*m* HCl/0.02 *m* NaCl 0.5*m* H_2SO_4/0.5*m* H_2SO_3	e.j. WL B ΔB-WL[a]	11919.3 11920.7 11931 10.3
cap 30 ***t*** = 485 °C, ***P*** = 700 bar ***d*** = 0.67 g·cm^{-} 3.4 *m* NaCl 0.7*m* H_2SO_4/0.6*m* H_2SO_3	e.j. WL B ΔB-WL[a]	11919.6 11920.8 11930.5 9.8
TFY-XANES (± 0.5 eV)		
cap 2156 **Melt** CsCl/NaCl/KCl 45.5at.%/30 at%/24.5 at% ***t*** = 650 °C	e.j. WL B	11919.5 11922.5 11935.5
cap 2156 **Crystallized melt** CsCl/NaCl/KCl **Ambient temperature**	e.j. WL B	11918 11920 11934
Cap110 ***t*** = 400 °C, ***P*** = 850 bar ***d*** = 0.71 g·cm^{-3} 3.8*m* HCl/0.57*m* KCl/ 0.03 *m* $K_2S_2O_8$	e.j. WL B	11919 11922 11931/11933
Cap110 ***t*** = 450 °C, ***P*** = 2100 bar	e.j. WL B	11919 11922 11931/11933
Cap117 ***t*** = 450 °C, ***P*** = 4500 bar ***d*** = 1.04 g·cm^{-3} 7.3*m* HCl/4.2*m* CsCl 0.56*m* H_2SO_4/0.12*m* Na_2SO_3	e.j. WL B	11919 11922 11931/11933
Cap118 ***t*** = 575 °C, ***P*** = 2100 bar ***d*** = 0.68 g·cm^{-3} 7.3*m* HCl/4.2*m* CsCl 0.56*m* H_2SO_4/0.12*m* Na_2SO_3	e.j. WL B	11919 11922 11932
Cap122 ***t*** = 350 °C, ***P*** = 150 bar ***d*** = 0.96 g·cm^{-3}, 3.8*m* HCl/7.2*m* KCl/ 0.4*m* $K_2S_2O_8$	e.j. WL B	11918.5 11921.5 11931/11933
Cap122 ***t*** = 400 °C, ***P*** = 500 bar	e.j. WL B	11918.5 11921.5 11930/11933
Cap122 ***t*** = 450 °C, ***P*** = 1100 bar	e.j. WL B	11918.5 11921.5 11930/11933
Cap122 ***t*** = 525 °C, ***P*** = 1900 bar	e.j. WL B	11918.5 11921.5 11931
[a] energy difference between maxima of B and WL features.		

Table 4. Results of EXAFS spectra fitting (ARTEMIS program, S_0^2 = 0.84, $AuCs_2Cl_6$ was accepted as initial model structure, Matsushita and Ahsbahs, 1998). Experimental spectra fits were performed in *k*-space if not indicated otherwise.

Atom	EXAFS				
	N	*R*, Å	σ^2, Å^{-2}	Fit quality	
				E°, eV	Red. chi^2 (R-factor)
Cap 2156, melt CsCl/NaCl/KCl (*k*-space: 3 – 13), ***t*** = 650 °C					
Cl	2	2.28±0.007	0.004±0.001	8.8±1.0	(0.033)
Cs	0.19±0.21	4.03±0.05	0.002±0.001		
MS[1]	2	4.60±0.05	0.021±0.009		
Cap 2156, crystallized melt CsCl/NaCl/KCl (*k*-space: 3 – 13), ambient temperature					
Cl	1.88±0.32	2.29±0.009	0.001±0.001	8.0±1.7	(0.060)
Cl	0.96±0.79	2.94±0.03	0.003±0.006		
Cs	1	3.26±0.08	0.012±0.011		
MS[1]	1.88	4.58±0.05	0.004±0.007		
MS[1]	0.96±0.79	5.08±0.05	0.003±0.022		
Cap110 (fit in *R*–space, *R* -range: 1.3-4.4; *k-range*: 3 – 11), ***t*** = 400 °C, ***P*** = 850 bar ***d*** = 0.71 g·cm^{-3}, 3.8*m* HCl/0.57*m* KCl/0.03 *m* $K_2S_2O_8$					
Cl	2.27±0.13	2.27±0.005	0.006±0.001	7.5±2.5	0.5 (0.007)
K	1	4.15±0.02	0.003±0.002		
MS[1]	2.27±0.13	4.53±0.02	0.016±0.004		
Cap110 (fit in *R*–space, *R* -range: 1.3-4.4; *k-range*: 3 – 10), ***t*** = 450 °C, ***P*** = 2100 bar					
Cl	2.08±0.23	2.26±0.009	0.004±0.001	7.2±1.2	3.0 (0.013)
K	1	4.12±0.07	0.004±0.06		
MS[1]	2.08±0.23	4.50±0.04	0.006±0.005		
Cap117 (fit in *R*–space, *R* -range: 1.3-4.4; *k-range*: 3 – 13), ***t*** = 450 °C, ***P*** = 4500 bar ***d*** = 1.04 g·cm^{-3}, 7.3*m* HCl/4.2*m* CsCl (+0.56*m* H_2SO_4/0.12*m* Na_2SO_3)					
Cl	2.02±0.13	2.25±0.005	0.004±0.001	4.6±0.8	1.3 (0.013)
Cs	0.59±0.86	4.11±0.03	0.005±0.007		
MS[1]	2.02±0.13	4.48±0.03	0.020±0.008		
Cap118 (fit in *R*–space, *R* -range: 1.3-4.4; *k-range*: 3 – 11), ***t*** = 575 °C, ***P*** = 2100 bar ***d*** = 0.68 g·cm^{-3}, 7.3*m* HCl/4.2*m* CsCl (+0.56*m* H_2SO_4/0.12*m* Na_2SO_3)					
Cl	1.76±0.26	2.27±0.01	0.003±0.001	6.6±1.6	13.7 (0.030)
Cs	0.30±0.63	3.31±0.05	0.003±0.013		
MS[1]	1.76±0.26	4.52±0.08	0.019±0.012		

Table 4 - continued

Cap122 (fit in *R*–space, *R* -range: 1.3-4.4; *k-range*: 3 – 13), ***t*** = 350 °C, ***P*** = 150 bar (possible presence of vapor bubble) ***d*** = 0.96 g·cm^{-3}, 3.8*m* HCl/7.2*m* KCl/0.4*m* $K_2S_2O_8$					
Cl	2.04±0.18	2.28±0.006	0.003±0.001	8.8±1.1	7.1 (0.022)
K	0.53±1.49	4.08±0.06	0.003±0.016		
MS[1]	2.04±0.18	4.54±0.08	0.018±0.009		
Cap122 (fit in *R*–space, *R* -range: 1.3-4.4; *k-range*: 3 – 10). ***t*** = 400 °C, ***P*** = 500 bar					
Cl	1.85±0.24	2.27±0.01	0.003±0.001	8.0±1.4	1.4 (0.026)
MS[1]	1.85±0.24	4.54±0.04	0.010±0.006		
Cap122 (*k-range*: 3 – 13). ***t*** = 450 °C, ***P*** = 1100 bar					
Cl	2.11±0.19	2.27±0.007	0.004±0.001	8.1±1.1	3.6 (0.024)
K	1	4.06±0.04	0.005±0.004		
MS[1]	2.11±0.19	4.49±0.04	0.016±0.008		
Cap122 (*k-range*: 3 – 12). ***t*** = 525 °C, ***P*** = 1900 bar					
Cl	1.93±0.19	2.27±0.008	0.004±0.001	7.5±1.2	3.9 (0.026)
K	1	3.97±0.02	0.014±0.016		
MS[1]	1.93±0.19	4.53±0.07	0.023±0.013		
[1] MS – multiple scattering, Au-Cl1-Au-Cl2.					

Table 5. Geometries of Au aqueous complexes obtained by the *ab initio* molecular dynamics (AIMD) simulations (simulation details are given in Table 2). Uncertainties correspond to the standard deviations. Cation coordination number *N* corresponds to number of cations inside a sphere with radius of 6 Å.

AIMD calculation	Fluid composition	Complex	Au-Cl, Å	Cl-Au-Cl, °	Cation *N*
A	2*m* HCl	$Au(Cl)_2^-$	2.35 (0.078)	167 (6.2)	-
B	2*m* NaCl	$Au(Cl)_2^-$	2.35 (0.065)	169 (5.6)	0.17
C	2*m* KCl	$Au(Cl)_2^-$	2.35 (0.074)	168 (5.8)	0.36
D	2*m* CsCl	$Au(Cl)_2^-$	2.35 (0.087)	169 (6.1)	0.41
E	4*m* CsCl	$Au(Cl)_2^-$	2.35 (0.078)	165 (8.0)	1.31
F	CsCl/NaCl/ KCl	$Au(Cl_2)^-$	2.40 (0.14)	159 (16.0)	8.32
G	4*m* CsCl	$Au(Cl_2)^-$	2.34 (0.076)	168 (7.0)	1.63

Figure captions

Fig. 1. Gold L_3-edge HERFD-XANES spectra of Au-bearing solutions (Cap28, 30) and melt (Cap5407). Vertical dashed lines indicate the main spectral features.

Fig. 2. Gold L_3-edge TFY-XANES spectra of: (a) - Au-bearing solutions (Cap110, 117, 118, 122) and melt (Cap2156), and (b) – melt (Cap2156) at 650 °C and after crystallization at ambient temperature.

Fig. 3. Comparison of experimental Au L_3-edge EXAFS spectra (*left*) and their Fourier Transforms (*right*).

Fig. 4. Results of Au L_3-edge EXAFS spectra fits performed by means of ARTEMIS program. (a) CsCl/KCl/NaCl melt (Cap2156). (b-d) Aqueous fluids cap110, cap117, 118, cap122. *Top* - normalized k^2-weighted EXAFS spectra; *Bottom* - corresponding Fourier Transforms (not corrected for phase shift). Thick black line – experimental spectra, thin dotted red line – fit. Experimental *TP*-parameters and fluid compositions are indicated at the top of each figure.

Fig. 5. Atomic densities and coordination numbers of Au complexes obtained using *ab initio* molecular dynamics (AIMD) simulations (see Table 2 for system compositions).

Fig. 6. EXAFS signal and wavelet transform (WT) of the EXAFS signal (distance R (Å) vs. wavevector k (Å^{-1})). (a) contributions of different scattering atoms to the EXAFS spectra, AIMD calculation E (4*m* CsCl). (b) experimental spectra cap117 and cap118. Not corrected for phase shift. The WT intensity scales are shown at the right side of each WT image.

Fig. 7. Gold L_3-edge HERFD-XANES spectra calculated using atomic configurations generated via AIMD simulations. Spectrum $AuCl_2H$ corresponds to calculation A, $AuCl_2Cs$ – calculation D, $AuCl_2Cs_4$ – calculation E, melt – calculation F. Compositions of simulation boxes are given in Table 2.

Fig. 8. Position of Cs calculated by AIMD (calculation E) (a), and positive Bader partial atomic charge of Au as a function of Au-Cs distance (b). Each point in Fig. (b) corresponds to average AIMD configuration for ±0.12 Å interval around the indicated Au-Cs distance.

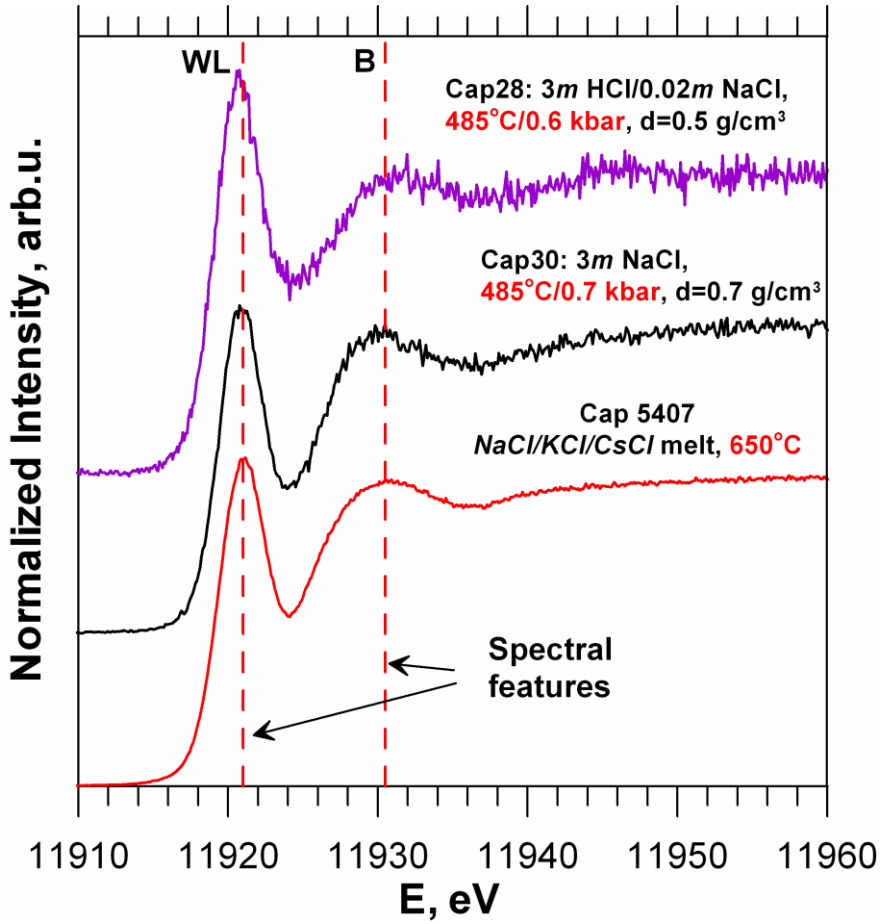
WL
B
Cap28: 3m HCl/0.02m NaCl,
485°C/0.6 kbar, d=0.5 g/cm³
Cap30: 3m NaCl,
485°C/0.7 kbar, d=0.7 g/cm³
Cap 5407
NaCl/KCl/CsCl melt, 650°C
Spectral
features
Normalized Intensity, arb.u.
11910
11920
11930
11940
11950
11960
E, eV

Fig. 1

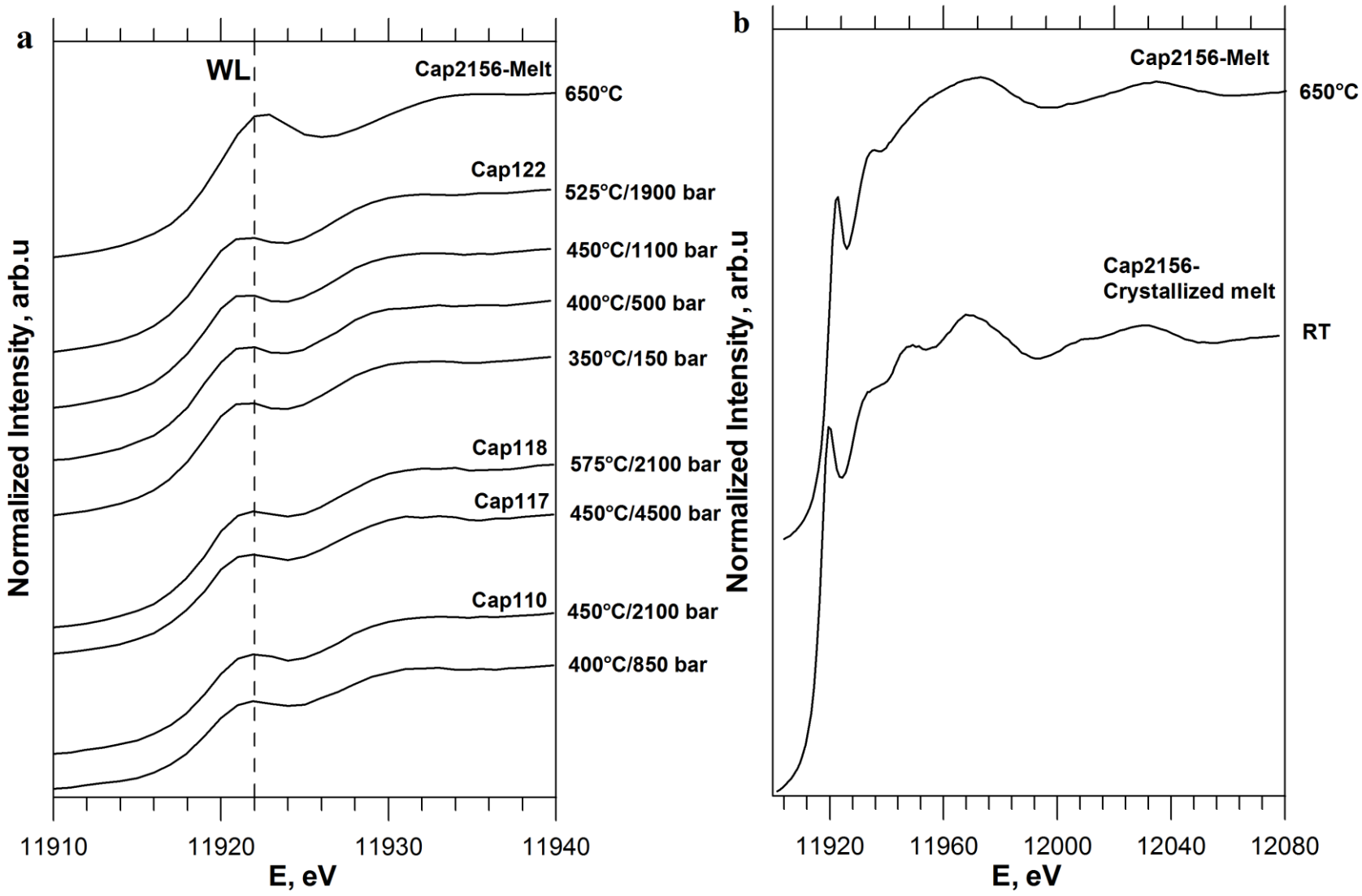
a
WL
Cap2156-Melt
650°C
Cap122
525°C/1900 bar
450°C/1100 bar
400°C/500 bar
350°C/150 bar
Cap118
575°C/2100 bar
Cap117
450°C/4500 bar
Cap110
450°C/2100 bar
400°C/850 bar
Normalized Intensity, arb.u
11910
11920
11930
11940
E, eV
b
Cap2156-Melt
650°C
Cap2156-
Crystallized melt
RT
Normalized Intensity, arb.u
11920
11960
12000
12040
12080
E, eV

Fig. 2

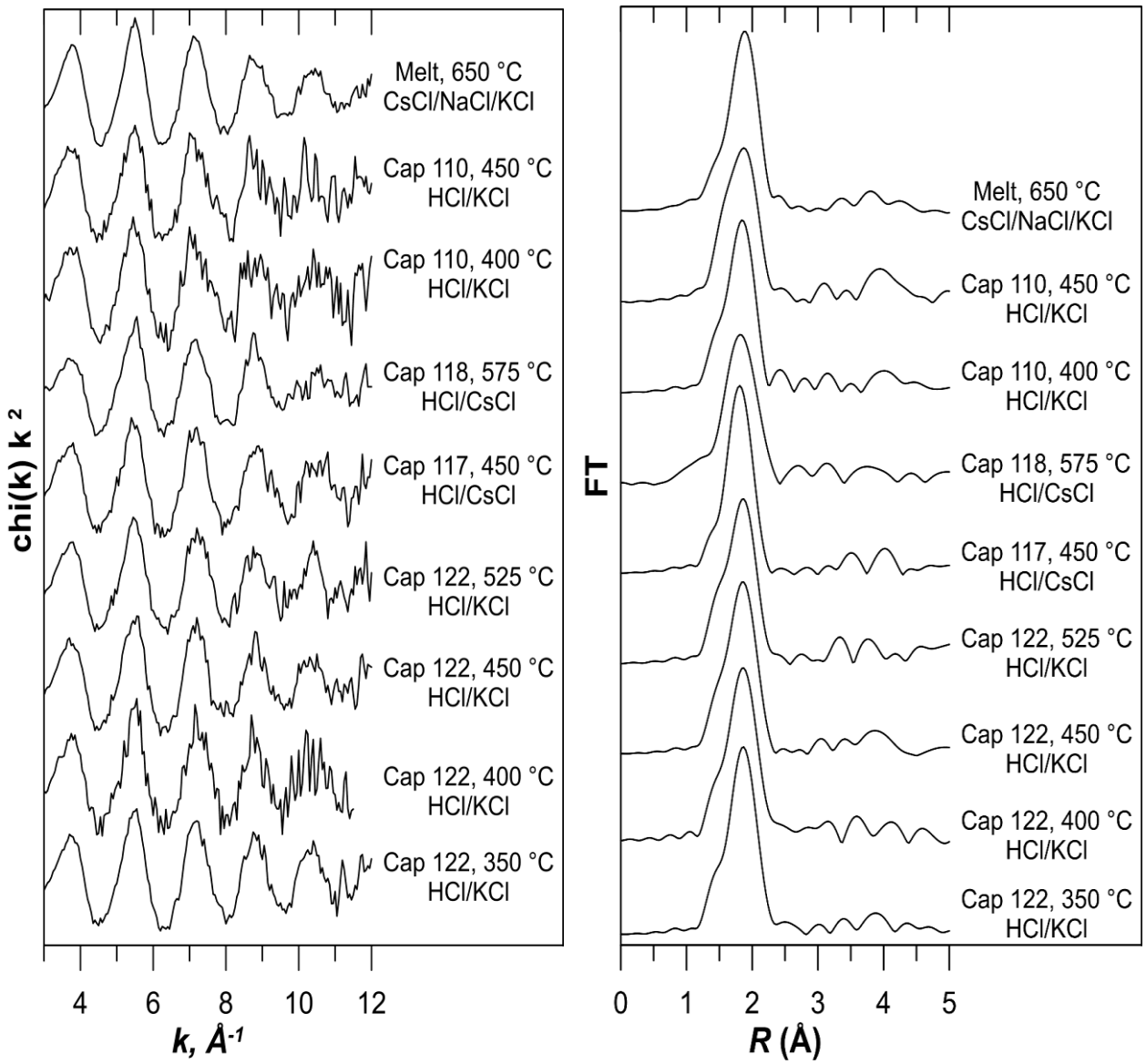
chi(k) k ²
k, Å-1
4
6
8
10
12
Melt, 650 °C
CsCl/NaCl/KCl
Cap 110, 450 °C
HCl/KCl
Cap 110, 400 °C
HCl/KCl
Cap 118, 575 °C
HCl/CsCl
Cap 117, 450 °C
HCl/CsCl
Cap 122, 525 °C
HCl/KCl
Cap 122, 450 °C
HCl/KCl
Cap 122, 400 °C
HCl/KCl
Cap 122, 350 °C
HCl/KCl
FT
R (Å)
0
1
2
3
4
5
Melt, 650 °C
CsCl/NaCl/KCl
Cap 110, 450 °C
HCl/KCl
Cap 110, 400 °C
HCl/KCl
Cap 118, 575 °C
HCl/CsCl
Cap 117, 450 °C
HCl/CsCl
Cap 122, 525 °C
HCl/KCl
Cap 122, 450 °C
HCl/KCl
Cap 122, 400 °C
HCl/KCl
Cap 122, 350 °C
HCl/KCl

Fig. 3

a

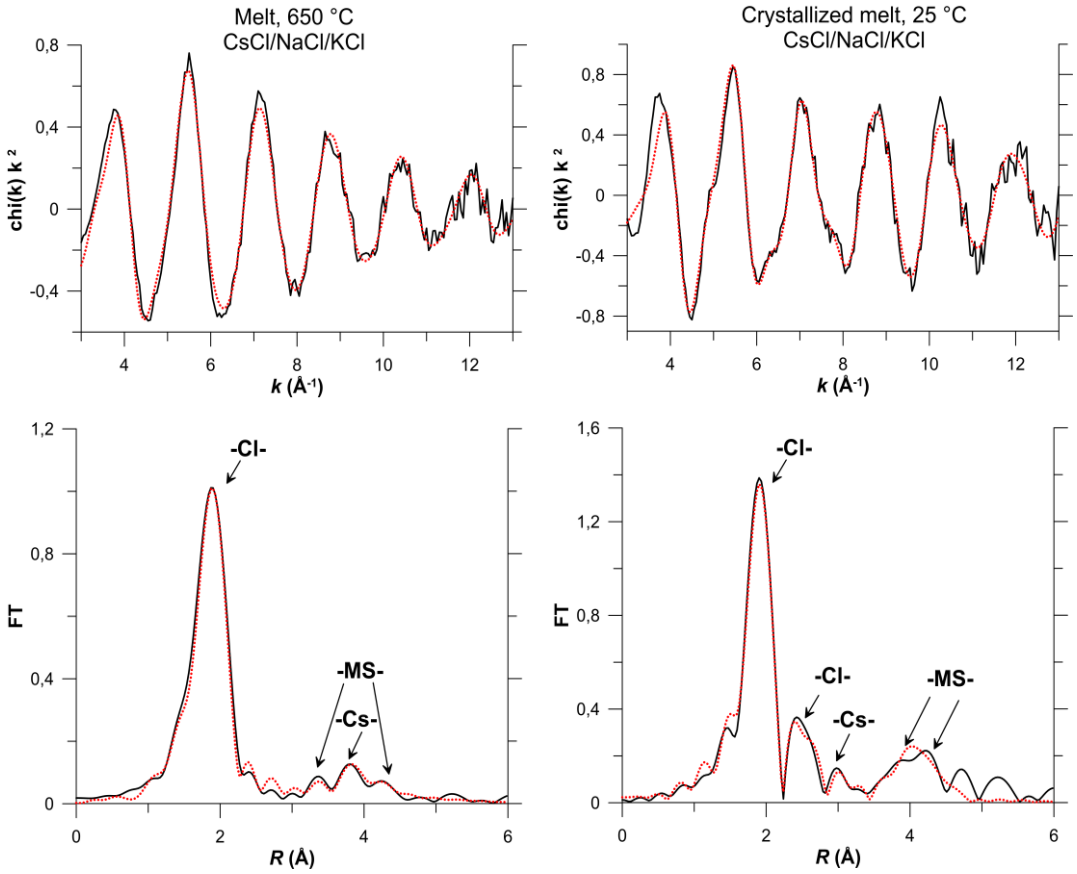
Melt, 650 °C
CsCl/NaCl/KCl
Crystallized melt, 25 °C
CsCl/NaCl/KCl
chi(k) k ²
k (Å⁻¹)
FT
R (Å)
-Cl-
-MS-
-Cs-

Fig. 4

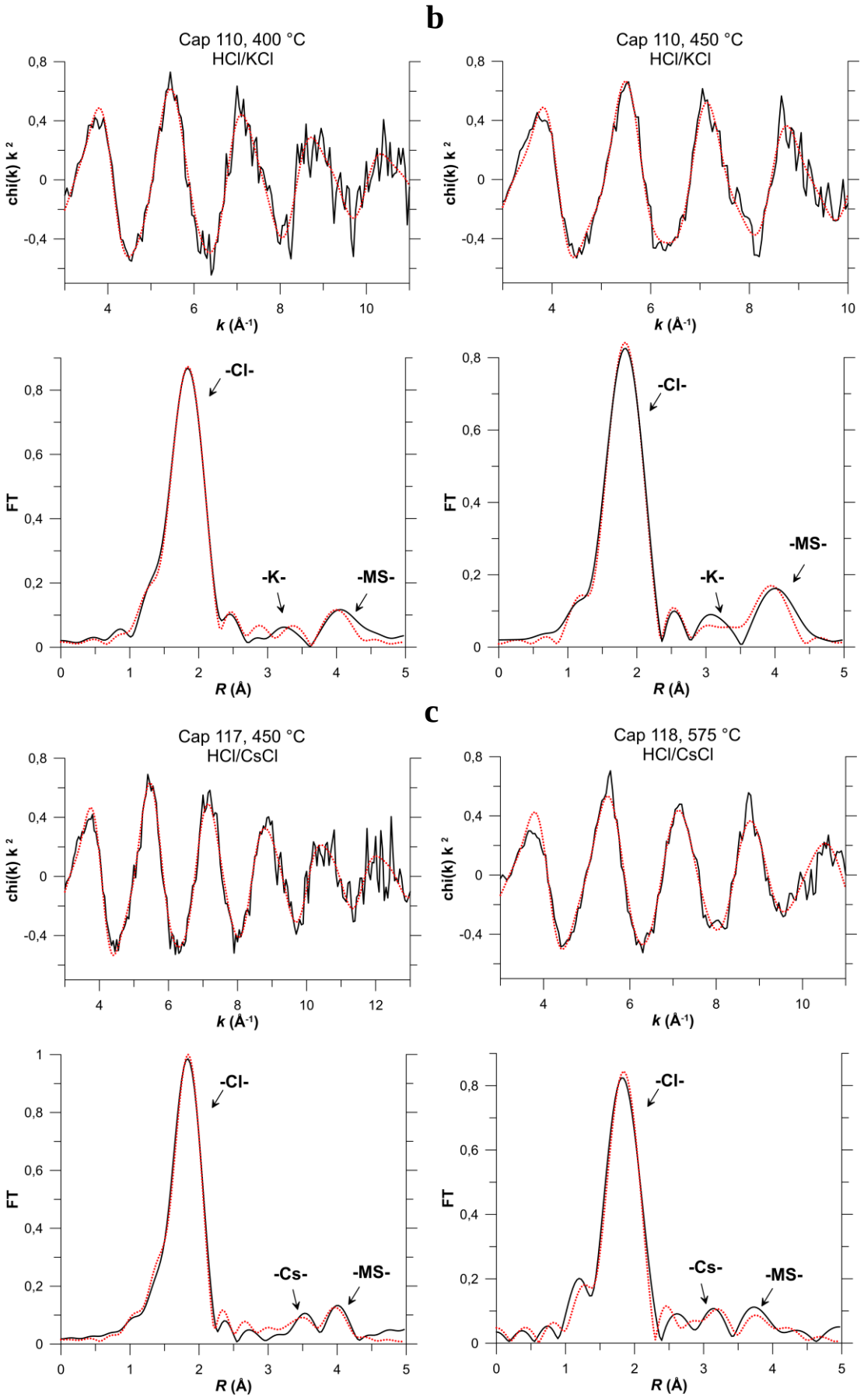

Fig. 4 - continued

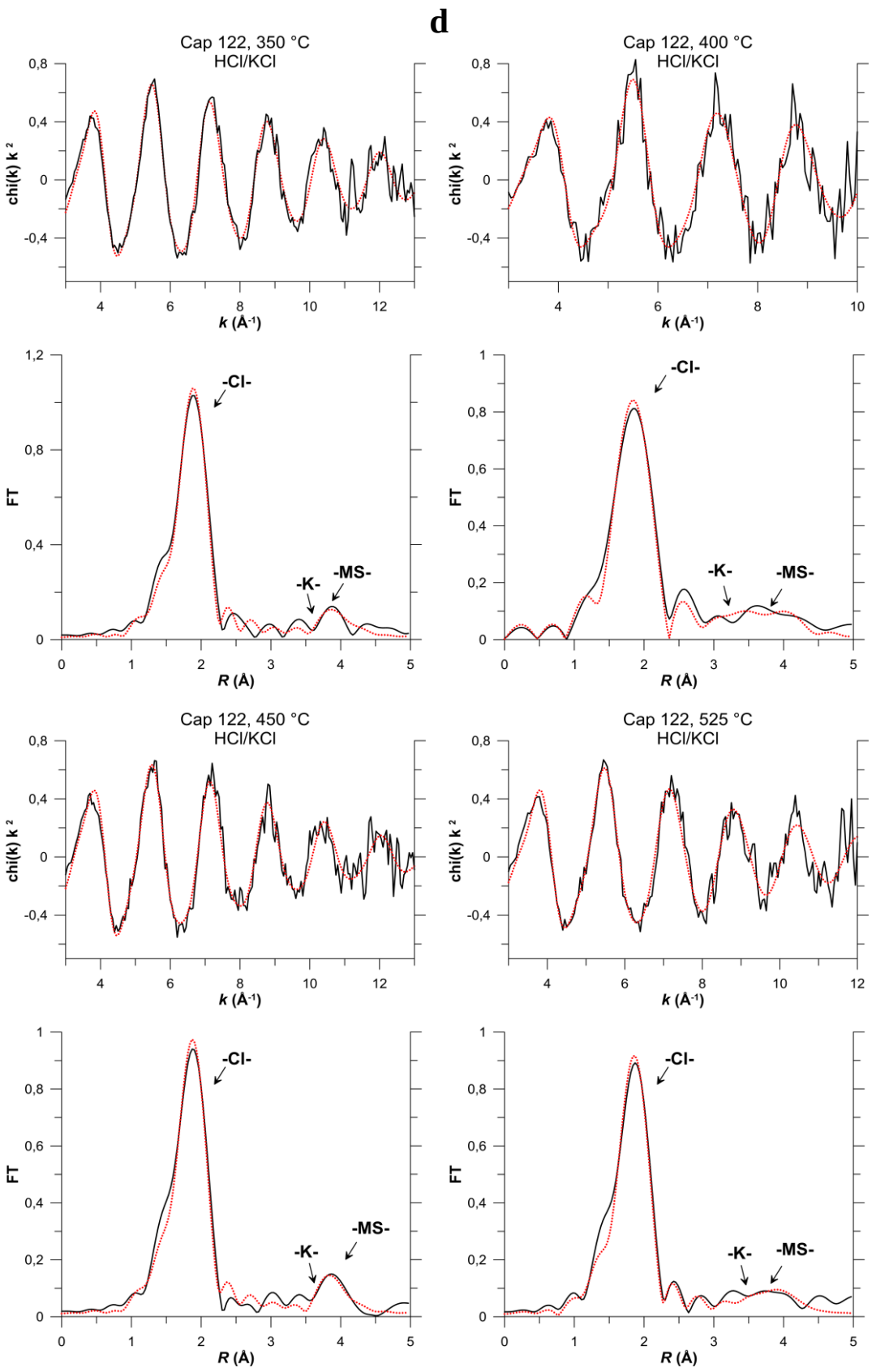

Fig. 4 – continued

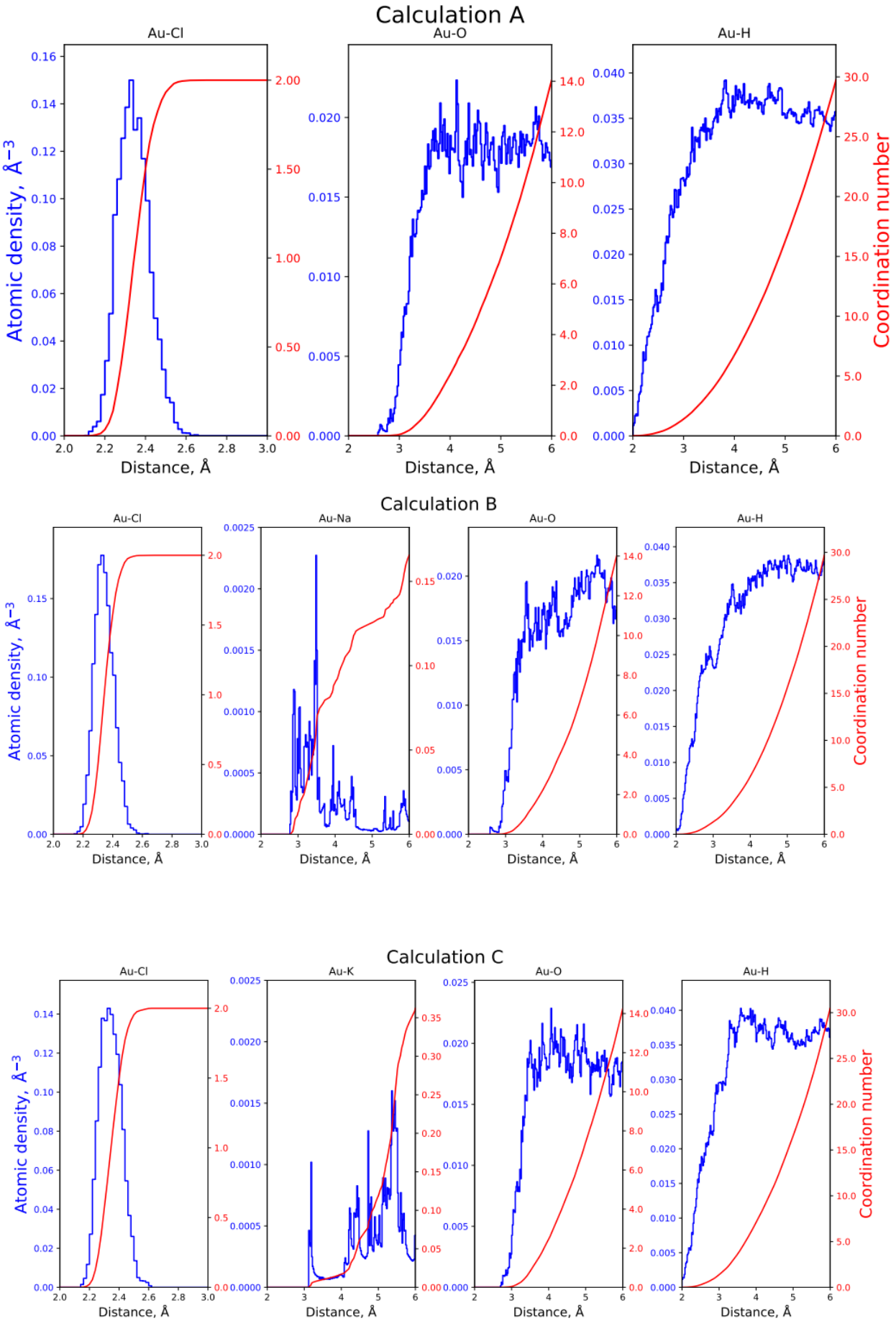
Calculation A
Au-Cl
Au-O
Au-H
Atomic density, Å⁻³
Coordination number
Distance, Å
Calculation B
Au-Cl
Au-Na
Au-O
Au-H
Atomic density, Å⁻³
Coordination number
Distance, Å
Calculation C
Au-Cl
Au-K
Au-O
Au-H
Atomic density, Å⁻³
Coordination number
Distance, Å

Fig. 5

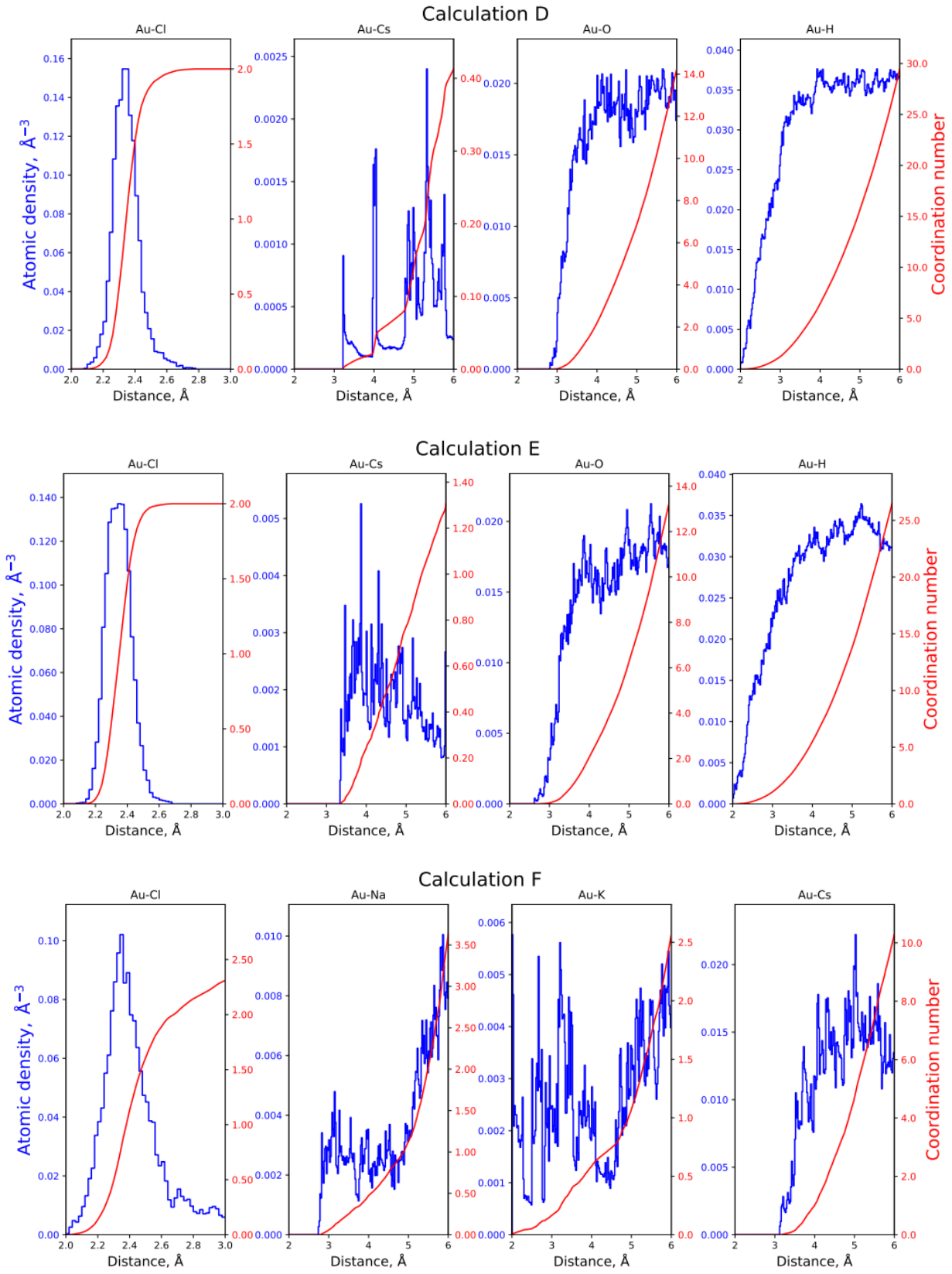

Fig. 5 – continued

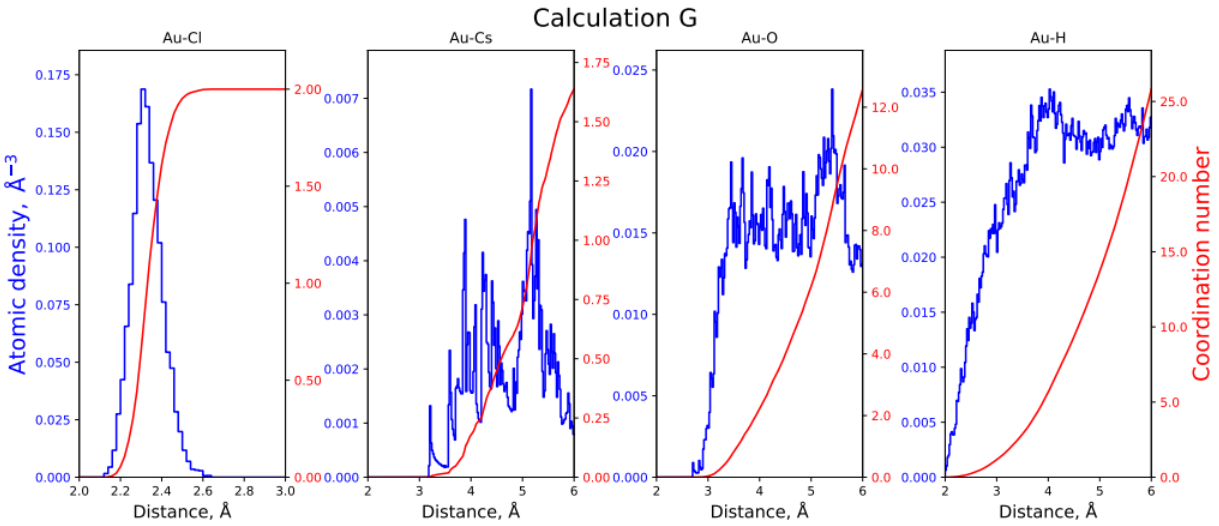

Fig. 5 – continued

Cl **a)** AIMD-EXAFS O

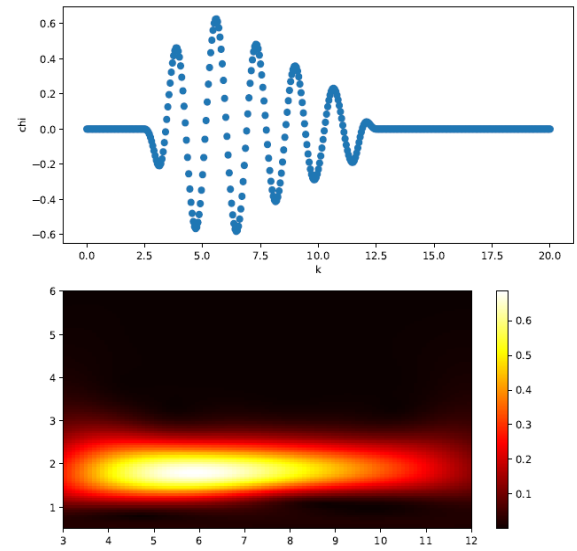

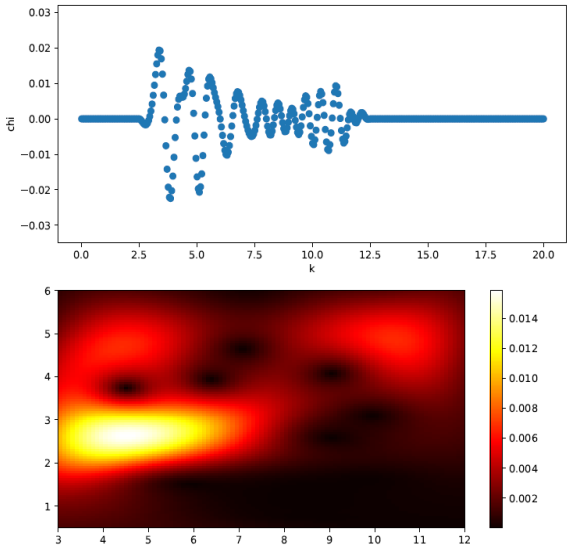

Cl-Au-Cl **Cs**

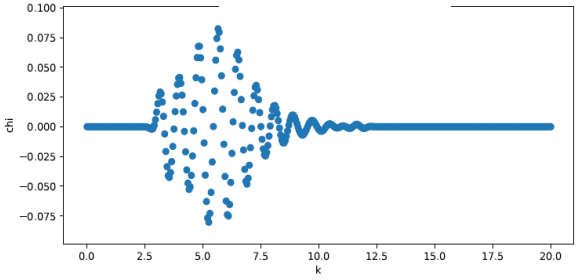

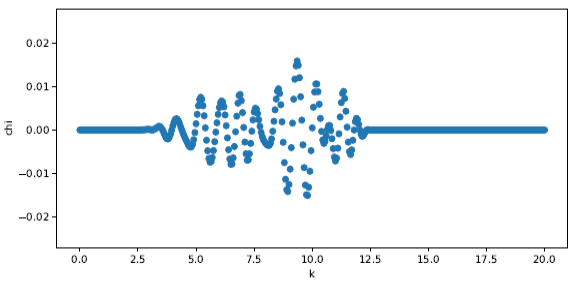

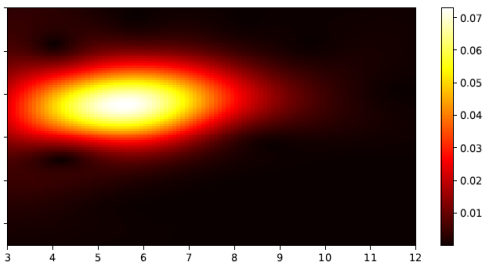

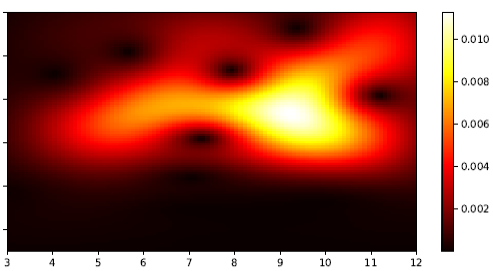

Cap 117, 450 °C/4500 bar **b)** Experiment **Cap 118, 575 °C/2100 bar**

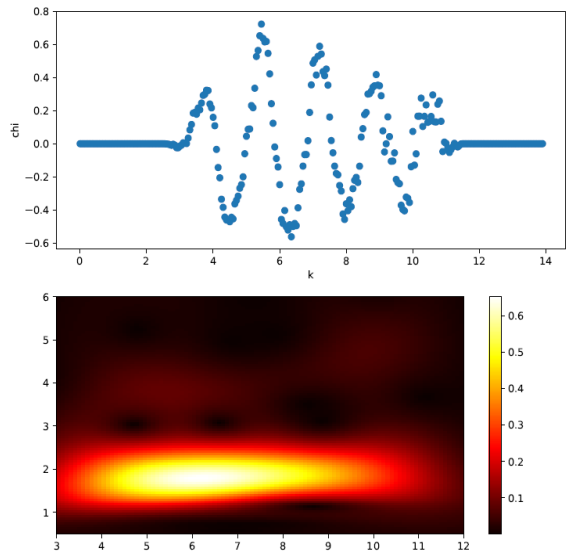

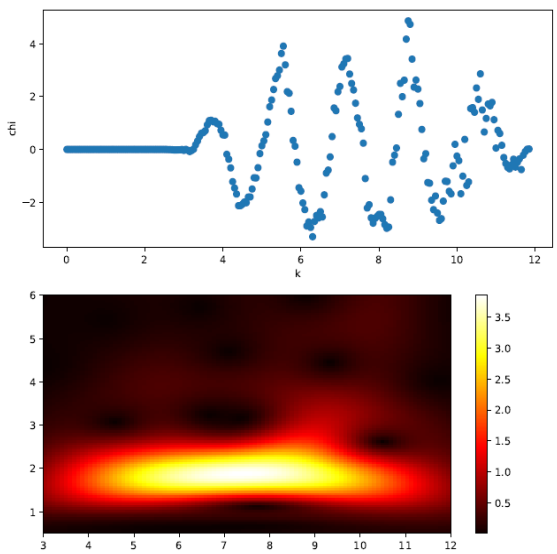

Fig. 6

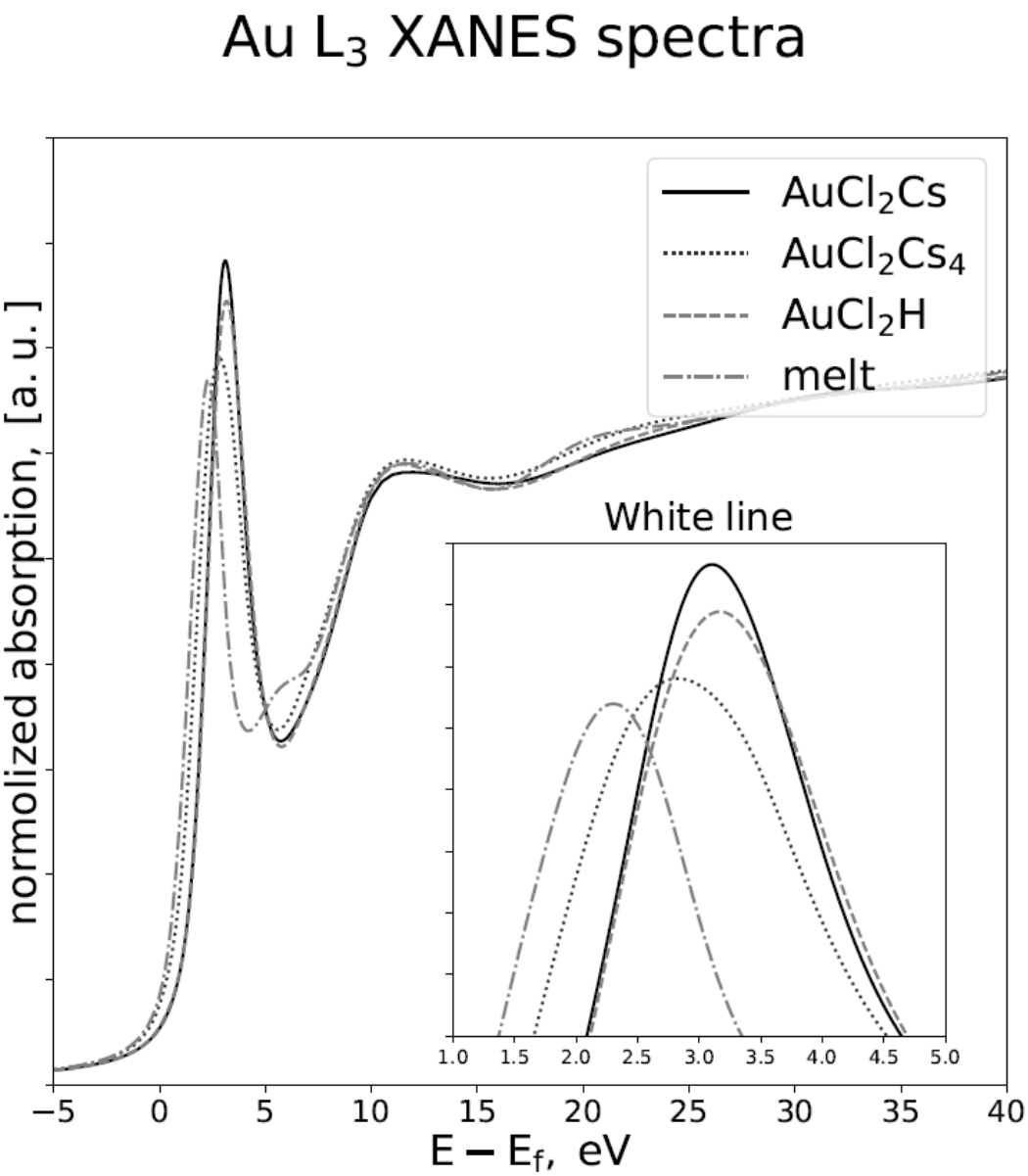
Au L_3 XANES spectra
$AuCl_2Cs$
$AuCl_2Cs_4$
$AuCl_2H$
melt
White line
normolized absorption, [a. u.]
$E - E_f$, eV

Fig. 7

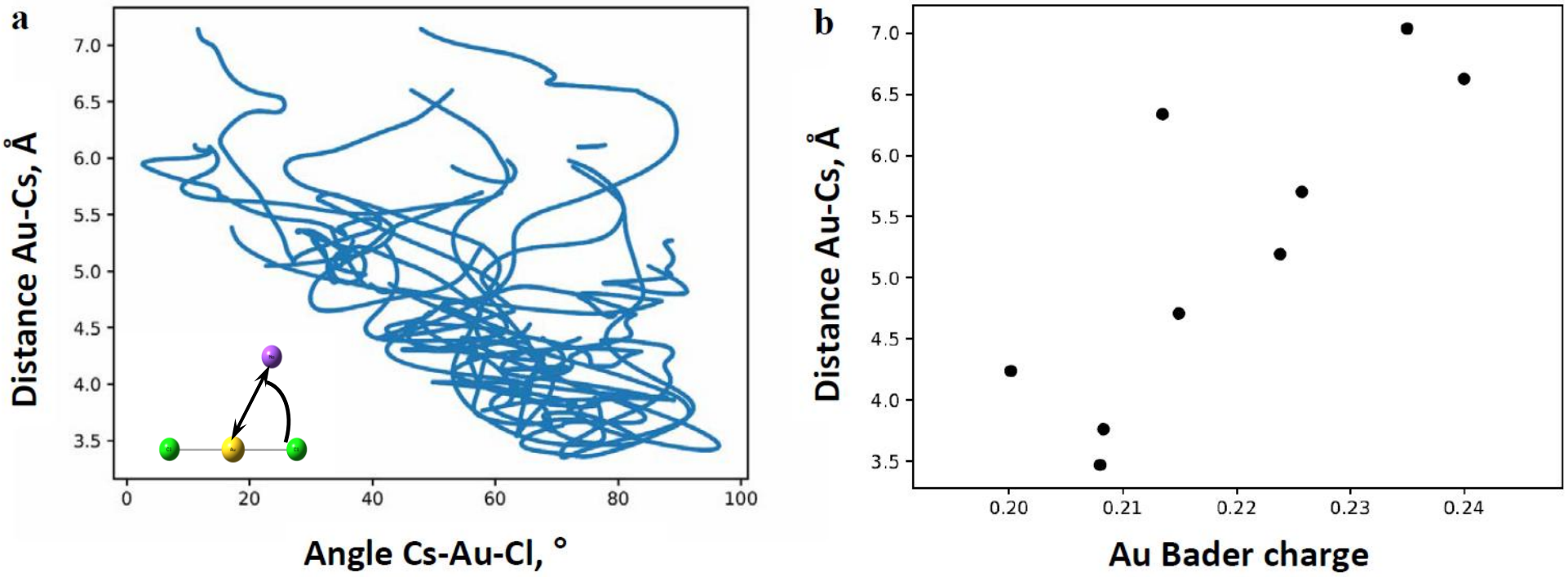
a
Distance Au-Cs, Å
Angle Cs-Au-Cl, °
b
Distance Au-Cs, Å
Au Bader charge

Fig. 8

Electronic Annex

Click here to download Electronic Annex: Electronic Supplement-14.pdf